SAND REPORT

SAND 2003-0698
Unlimited Release
Printed March 2003

Long-term Pumping Test at MIU Site, Toki, Japan: Hydrogeological Modeling and Groundwater Flow Simulation

Mehdi Eliassi and Sean A. McKenna

Prepared by

Sandia National Laboratories

Albuquerque, New Mexico 87185 and Livermore, California 94550

Sandia is a multiprogram laboratory operated by Sandia Corporation,
a Lockheed Martin Company, for the United States Department of Energy's
National Nuclear Security Administration under Contract DE-AC04-94-AL85000.

Issued by Sandia National Laboratories, operated for the United States Department of Energy by Sandia Corporation.

Available to DOE and DOE contractors from
U.S. Department of Energy
Office of Scientific and Technical Information
P.O. Box 62
Oak Ridge, TN 37831

Telephone: (865)576-8401
Facsimile: (865)576-5728
E-Mail: reports@adonis.osti.gov
Online ordering: http://www.doe.gov/bridge

Available to the public from
U.S. Department of Commerce
National Technical Information Service
5285 Port Royal Rd
Springfield, VA 22161

Telephone: (800)553-6847
Facsimile: (703)605-6900
E-Mail: orders@ntis.fedworld.gov
Online order: http://www.ntis.gov/help/ordermethods.asp?loc=7-4-0#online

SAND2003-0698
Unlimited Release
Printed March, 2003

Long-term Pumping Test at MIU Site, Toki, Japan: Hydrogeological Modeling and Groundwater Flow Simulation

Mehdi Eliassi and Sean A. McKenna
Geohydrology Department
Sandia National Laboratories
P.O. Box 5800
Albuquerque, NM 87185-0735

Abstract

A conceptual model of the MIU site in central Japan, was developed to predict the groundwater system response to pumping. The study area consisted of a fairly large three-dimensional domain, having the size 4.24 x 6 x 3 km^3 with three different geological units, upper and lower fractured zones and a single fault unit. The resulting computational model comprised of 702,204 finite difference cells with variable grid spacing. Both steady-state and transient simulations were completed to evaluate the influence of two different surface boundary conditions: fixed head and no flow. Steady state results were used for particle tracking and also serving as the initial conditions (i.e., starting heads) for the transient simulations. Results of the steady state simulations indicate the significance of the choice of surface (i.e., upper) boundary conditions and its effect on the groundwater flow patterns along the base of the upper fractured zone. Steady state particle tracking results illustrate that all particles exit the top of the model in areas where groundwater discharges to the Hiyoshi and Toki rivers. Particle travel times range from 3.6×10^7 sec (i.e., ~1.1 years) to 4.4×10^{10} sec (i.e., ~1394 years). For the transient simulations, two pumping zones one above and another one below the fault are considered. For both cases, the pumping period extends for 14 days followed by an additional 36 days of recovery. For the pumping rates used, the maximum drawdown is quite small (ranging from a few centimeters to a few meters) and thus, pumping does not severely impact the groundwater flow system. The range of drawdown values produced by pumping below the fault are generally much less sensitive to the choice of the boundary condition than are the drawdowns resulted from the pumping zone above the fault.

Acknowledgements

This work was done under funding from the Japanese Nuclear Cycle Development Institute (JNC) and the authors are indebted to Mr. Nakano, Mr. Takeuchi and Mr. Saegusa of the JNC Tono Geoscience Center for initiating the funding and for support during this project. Additionally, Mr. Saegusa, Mr. Takeuchi and Mr. Inaba provided helpful comments on this report.

Sandia is a multiprogram laboratory operated by Sandia Corporation, a Lockheed Martin Company, for the United States Department of Energy's National Nuclear Security Administration under contract DE-AC04-94-AL-85000

Table of Contents

Abstract 4
Acknowledgements 5
Table of Contents 6
Introduction 10
Theory 11
Conceptual Model Development 12
Model Geology and Hydraulic Properties 13
Effective Hydraulic Conductivity of the Tsukyoshi Fault 14
Numerical Mesh 16
Initial and Boundary Conditions 18
Results of Steady-State and Transient Simulations 20
Steady-state Simulations 20
Long-term Pumping Test Simulations 29
Wellbore correction 33
Drawdown as a measure of groundwater performance 33
Illustrative Particle Tracking for LTPT 41
Conclusions 46
References 47

List of Figures

Figure 1. Plan view of the H-13 conceptual model boundaries in the North-East directions..... 12

Figure 2. Cross-sectional view in the Y-Z plane illustrating the three different geological units used for the H-13 model. The colors represent the hydraulic conductivity values used for each unit where, orange is the upper unit, blue is the lower unit, and green is the fault. The yellow boxes also represent the two pumping well locations above and below the fault to be used for transient simulations. 13

Figure 3. The effective hydraulic conductivity of the fault region (red line) and the model domain (blue line) as calculated with (3). The green and magenta horizontal lines denote the elevation of the ground surface and the upper fractured zone/sedimentary unit – lower fractured zone contact respectively..... 16

Figure 4. Representative views of the computational grid used to discretize H13 conceptual model: a) plan view in XY-plane illustrates the finer grid spacing used near and around the pumping well and b) typical transect in the YZ plane shows the variations in the topography near the surface. 17

Figure 5. Plan view for layer 4 exemplifying the implementation of elevation dependent topography using MODFLOW active node option. 19

Figure 6. Typical plan view illustrating initial (starting) head field for the H13 model..... 19

Figure 7. Computed steady-state head field in the YZ transect near the pumping well locations using fixed head surface boundary condition. 20

Figure 8. Computed steady-state head field in the YZ transect near the pumping well locations using no flow surface boundary condition..... 21

Figure 9. Darcy flux vectors for the same location as Figures 7 and 8, illustrating the effect of: a) fixed head top boundary condition and b) no flow top boundary condition..... 22

Figure 10. Map of fluxes at the upper surface of the model. 24

Figure 11. Path lines for the steady-state particle tracks for the same transect as Figure 7, with the steady-state head values also plotted in the background. In general, particles released from both sides of the fault move up toward the surface. The horizontal flow occurring at the base of the high *K* layer also shows the implicit recharge arising from imposing constant head on the top boundary..... 26

Figure 12. 3-D images of the particle tracks under steady-state conditions. The color scale indicates log10 travel time in years (upper image), log10 Darcy velocity in m/sec (middle image) and log10 pore velocity in m/sec (lower image)..... 28

Figure 13. Total travel length and Darcy time versus particle number for the steady-state simulation..... 29

Figure 14. Contour lines for the head field after 14 days of pumping the well above the fault, with the hydraulic conductivity for the three geological units included in the background. Contrasting these results with the steady-state results (i.e., Figure 7), pumping appears to minimally impact the groundwater response. 30

Figure 15. Close-up view of the drawdown contours for the results discussed in Figure 13, illustrate the maximum drawdown (red color) is ~6 cm. Black line shows approximate location of Tsukioshi fault. 31

Figure 16. Close-up views of the drawdown contours after 14 days of pumping the lower well in: a) the YZ-plane, b) XZ-plane, and c) XY-plane indicate a maximum drawdown of ~2.5 m. The influence of the fault can be clearly seen in the YZ and XY transect. The black line shows the approximate location of the Tsukioshi Fault in the upper and lower images. 32

Figure 17. Corrected drawdown versus time, using fixed head top boundary condition, for the single well zone below and the four well zones above the fault. While the well zone above the fault yields a maximum drawdown of ~3.5 m, the maximum drawdown for each of the well zones above the fault are ~1 m. The sharp drop after 14 days indicates the end of pumping period, followed by the nearly full recovery at the end of 50-day period. Note that, during the recovery phase, the well zone below the fault shows a shallower drop off in slope 34

Figure 18. Corrected drawdown versus time for 14 days of pumping, illustrating the effects of top boundary condition (i.e., fixed head versus no flow), choice of layer's confinement, and reduced specific storage for: a) pumping above the fault and b) pumping zone below the fault. Note that in both figures, drawdown for constant head and no flow with all confining layers are not only identical, they also reach a constant value within ~2 days of pumping. However, the drawdown for the no flow case where the layers are treated as confined-unconfined is an increasing function of time. 36

Figure 19. Temporal variation of the corrected drawdown and its comparison to its derivative with respect to time for the pumping zone below the fault. The figure is focused near the end of the pumping period (i.e., t=14) and the onset of the recovery period to illustrate where the derivative experiences its largest change. 41

Figure 20. Typical backward particle tracking for a number of particles released from the pumping zone above the fault, for the no flow top boundary condition. Note that the maximum lengths of the path lines are consistent with the maximum zone of influence for the draw down (i.e., 10-20 m). Note that the figure is zoomed to near the pumping location to better illustrate the path lines 42

Figure 21. Close up views of the backward particle tracking started from the pumping zone below the fault, illustrating the effect of porosity reduction: a) baseline porosity value results path lengths on the order of 10-20 m, b) an order of magnitude reduction increases the path lines to roughly 150 m, and c) two orders of magnitude reduction in porosity increases the maximum path length to ~400 m. Note that for each case, as the baseline porosity is decreased, the figure is further zoomed out, which can be clearly seen through the thinning of the fault widths. 43

Figure 22. Forward particle tracks illustrating the effect of artificial porosity reduction on the path lengths: a) path lines using the baseline porosity values show near negligible movement away from where the particles are released from, b) a uniform reduction of 10% in porosity increases the path lengths to several meters, c) decreasing the baseline porosity further (e.g., 100% reduction) increases the path lengths to 100s of meters, and d) shows the plan view of the path lines for the case shown in c. 45

List of Tables

Table 1. Baseline hydraulic properties for the three geological units used in H-13 work..... 14

Table 2. Summary of model surface fluxes. 23

Table 3. JNC assigned and model particle locations used to evaluate flow paths behavior..... 25

Table 4. Path lines for the 24 particles listed in Table 2. In addition to the path lines coordinates, the travel distance, travel time, Darcy velocities, and the average porosity values are also included. 27

Table 5. LAYCON parameter values in MODFLOW (Harbaugh and Mcdonald, 1996) 37

Table 6. Performance measures indicating maximum drawdown ($DD_{\max}$), maximum drawdown time ($T_{DD,\max}$), and the time at which the first derivative of drawdown with respect to time becomes maximum ($\Delta T_{DD,\max}$), for various well locations. 39

Introduction

The Japan Nuclear Cycle Development Institute (JNC) has been conducting a series of pumping tests at the MIU site, located near the town of Mizunami in the Gifu Prefecture northeast of Nagoya City, Japan. It is noted that the MIU site, as discussed in this report, is now known as the Shobasama Site and is not to be confused with the new MIU site that began operations in late 2001. Sandia National Laboratories (SNL), as a member of five independent modeling groups, is responsible for developing conceptual hydrogeological models of the MIU site to numerically simulate the groundwater response to the pumping tests. However, detailed site geological information is not well known. In particular, in light of various fault zones that are not fully characterized, uncertainty analysis has become a major theme of the numerical modeling studies.

During the FY 2000 (also known as H-12), our focus was primarily on exploring the effects of five different conceptual fault models on steady state groundwater flow and the subsequent particle tracking. For the H-12 work, we considered PorSalsa, a three-dimensional (3D), finite-element (FE) based, nonisothermal flow and transport model, specifically developed for fast parallel computing (Martinez et al., 2001). The 3D model developed for the H-12 used nearly 10^6 FE nodes and the simulations were conducted on 20 nodes of a 36-node Linux-based cluster, with each simulation taking roughly six minutes to complete. Details of H-12 work are documented in McKenna et al. (2001).

For FY 2001 (i.e., H-13) modeling activities, we considered the Groundwater Modeling System (GMS) software package (GMS v3.1, 2000). GMS is a highly versatile graphically oriented package and is specially suited for developing and studying site-specific conceptual models. One of the groundwater flow simulators within GMS is MODFLOW, a modular 3D finite difference (FD) based model for simulating groundwater flow (e.g., see McDonald and Harbaugh, 1988). We also use MODPATH (Pollock, 1994) to track particles and compute the 3D path lines, for either steady-state or transient MODFLOW simulations.

The H-13 activities are essentially a continuation of the steady-state flow models that were conducted during the H-12 tasks. However, the main objective of H-13 work is to numerically predict the long-term pumping tests (LTPT) that are planned to be conducted at the MIU site. To accomplish this, we extend the H-12 model and use the GMS package to develop a fairly detailed 3D regional scale model. We first perform a series of steady-state simulations (without pumping) and examine the groundwater response by tracking the travel times and velocity of 24 different particles. We then use the simulated steady-state head fields as the initial condition and simulate the effects of pumping wells on the groundwater response. The resulting LTPT predictions will be discussed as drawdown maps and head values as a function of time, at certain piezometer locations.

Theory

The mathematical model describing the 3D transient groundwater flow can be stated as (e.g., see McDonald and Harbaugh, 1988) as:

$$S_s \frac{\partial h}{\partial t} = \frac{\partial}{\partial x}\left(K_{xx} \frac{\partial h}{\partial x} \right) + \frac{\partial}{\partial y}\left(K_{yy} \frac{\partial h}{\partial y} \right) + \frac{\partial}{\partial z}\left(K_{zz} \frac{\partial h}{\partial z} \right) - Q \qquad (1)$$

where S_s [1/L] is the specific storage, h [L] is the potentiometric head, x, y, and z [L] refer to the coordinate axes in each direction, K_{xx}, K_{yy}, and K_{zz} [L/T] are the hydraulic conductivity along the x, y, and z coordinates, respectively, and Q [1/T] is a volumetric flux per unit volume and represents water source and/or sink.

Naturally, when considering steady-state cases the left-hand side of (1) is identically zero, and we assume that there are no source/sink term (i.e., Q=0). For the transient cases, we evaluate the specific storage, S_s, using (Domenico and Schwartz, 1990) as:

$$S_s = \rho_w g(\beta_p + \phi\beta_w) \qquad (2)$$

where ρ_w (M/L^3) is density of water, g (L/T^2) is acceleration due to gravity, β_p (LT^2/M) is the rock compressibility, ϕ is the rock porosity, and β_w (LT^2/M) refers to the compressibility of water.

We note that the partial differential equation, (1), in combination with a set of initial and boundary conditions comprise the mathematical representation of groundwater flow. Moreover, S_s, K_{xx}, K_{yy}, K_{zz}, and Q may be functions of position (i.e., x, y, and z), with Q also varying with time, which makes (1) inherently nonlinear. Since under nonlinear conditions, an analytical solution for (1) is not generally available, this equation must be solved numerically. In this work, we use MODFLOW as our numerical simulator. The details of numerical approach used in MODFLOW can be found in McDonald and Harbaugh (1988).

Conceptual Model Development

For the H-13 work, the study area consists of a 4.25 x 6 x 3 km^3 domain in the X-, Y-, and Z-directions, respectively. **Figure 1** depicts the plan view of the conceptual model in the East-West (E-W) (i.e., X-direction) and North-South (N-S) (i.e., Y-direction) coordinates. The third dimension (i.e., Z-direction) is simply generated by extruding the X-Y plane in the Z-direction. The pumping well used in this study is located at the MIU site (i.e., X=5433.3 m and Y=-68455.29 m). One of the pumping zones is located above and another below the Tsukiyoshi fault (see also **Figure 2**). With respect to the ground level, the well screen above the fault extends approximately from -541.745 m to -641.745 m in the Z-direction and the pumping zone below the fault roughly extends from -747.845 to -776.245 m.

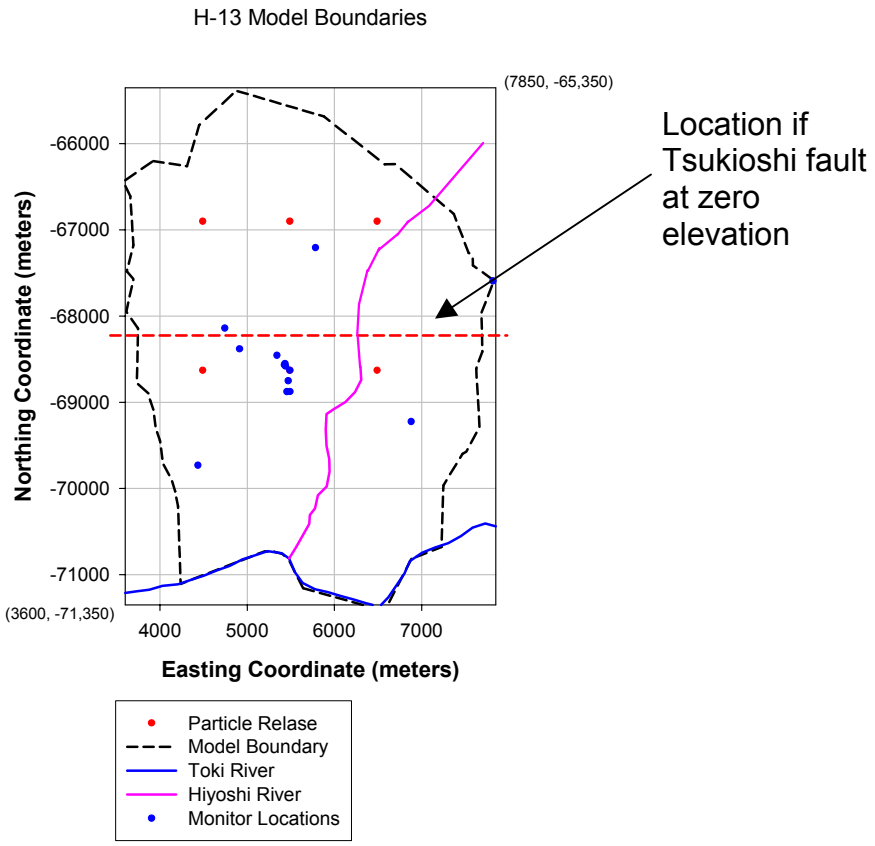

Figure 1. Plan view of the H-13 conceptual model boundaries in the North-East directions

Model Geology and Hydraulic Properties

The model considered here consists of three different geological units. **Figure 2** illustrates a cross-sectional view of these three units in Y-Z plane. The first unit is the upper fractured domain/sedimentary unit, where we have grouped the upper fractured zone and the sedimentary units together as a single hydrogeologic unit. The second unit is the lower fractured unit with lower hydraulic conductivity (K) and porosity (ϕ) than those of the upper unit. We should note that, the contact between the upper and lower fracture units is at an elevation of -120 m. Finally, the third geological unit is a fault zone (i.e., Tsukiyoshi fault) and is comprised of fairly low K and ϕ materials. **Table 1** lists the baseline hydraulic property values used in this study.

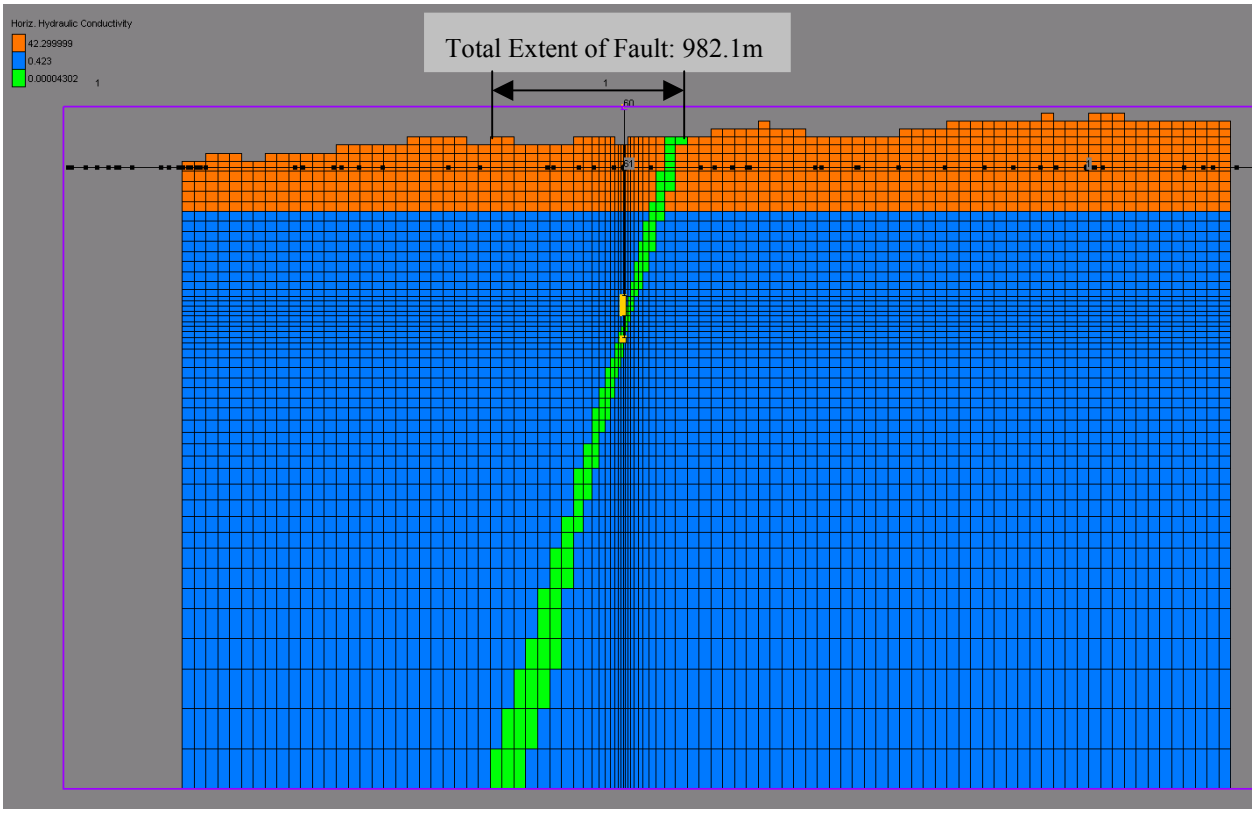

Figure 2. Cross-sectional view in the Y-Z plane illustrating the three different geological units used for the H-13 model. The colors represent the hydraulic conductivity values used for each unit where, orange is the upper unit, blue is the lower unit, and green is the fault. The yellow boxes also represent the two pumping well locations above and below the fault to be used for transient simulations.

Table 1. Baseline hydraulic properties for the three geological units used in H-13 work.

Geological Unit	K	ϕ	β_p	S_s	S_y
	(m/sec)	(-)	(m^2/N)	(1/m)	(-)
Upper Fractured	4.9×10^{-4}	0.1	7.6×10^{-9}	7.48×10^{-5}	0.08
Lower Fractured	4.9×10^{-6}	0.01	4.8×10^{-10}	4.94×10^{-6}	0.008
Fault	4.9×10^{-10}	0.005	4.8×10^{-10}	4.91×10^{-6}	0.004

The hydraulic conductivity values, listed in **Table 1**, are approximate values based on packer tests done in the MIU boreholes over 100 meter intervals. The K values used here are slightly higher than the hydraulic test results. This increase is based on an assumption of non-radial flow to the well (flow dimension less than 2.0) where the actual K being tested is higher than the average K that is assigned for a hydraulic test with an assumption of radial flow. At this time, there are no available data on fracture porosity for the MIU site and the assumed values are also approximate values taken from published results for other fractured rocks. To find the rock compressibility, β_p of the lower sedimentary and fault units, we use the midrange value for fissured rocks (Domenico and Schwartz, 1990, pg. 111). For the upper sedimentary unit β_p listed in **Table 1** is based on the midrange value for dense sandy gravel (Domenico and Schwartz, 1990, pg. 111). Thus, to calculate specific storage, S_s, we use (2) and choose ρ_w=997 kg/m^3, g=9.81 m/sec^2, and $\beta_w = 4.8 \times 10^{-10}$ m^2/N, where the β_w value is for water at 25 degrees C (see, Domenico and Schwartz, 1990, pg. 105). Finally, we simply assume the specific yield, S_y, to be 80% of the porosity for each geological unit.

Effective Hydraulic Conductivity of the Tsukioshi Fault

The hydraulic conductivity value assigned to the Tsukiohsi Fault is a constant value of 4.9×10^{-10} m/s. However, the discretization of the fault within the MODFLOW grid causes the thickness of the fault to vary from one layer of the model to the next. In order to determine the effect of this varying width on the general behavior of the fault, the effective hydraulic conductivity of the fault is calculated for each layer. These calculations are done on a Y-Z cross-section at the X coordinate of the MIU-2 borehole. The effective hydraulic conductivity, K_{eff}, of a given layer is determined by:

$$K_{eff} = \frac{W_{region}}{\frac{W_{fault}}{K_{fault}} + \frac{W_{background}}{K_{background}}} \qquad (3)$$

where W (L) is the width of either the region being examined, the fault, or the background (non-fault) material within each layer of the model and K is the hydraulic conductivity of the corresponding material. Keep in mind that the effective K is a calculation of the effective or average K of a region and that this region includes both fault and non-fault material.

The effective hydraulic conductivity calculation is made in two different ways. First, the effective K for each layer as extended across the entire model domain (W_{region} = 6000 m) is calculated. The second calculation is done for just the region of the model that contains the fault. This region extends from a Y coordinate of -69,221.0 m to -68,238.9 m, or a total width for this region of 982.1 m (Figure 2). The results of these calculations are shown in **Figure 3**. In this figure, the effective hydraulic conductivity of every layer containing a fault cell is calculated even though some of these layers are above the ground surface (see dashed green line). The average thickness of the fault in the model is 74.4 meters.

The results in this figure also show that the effective hydraulic conductivity of the region is quite sensitive to the discretization of the fault. From one layer to the next, the effective hydraulic conductivity of the region containing the fault can change by almost one-half of an order of magnitude. The reason for these abrupt changes is the stair-step nature of the fault discretization in the model. For some layers, the fault is 2 grid blocks thick and in the next layer, the fault is only a single grid block thick. These changes in the number of grid blocks defining the fault have a significant impact on the K_{eff} of the fault region. The figure also shows that the highest effective hydraulic conductivity of the fault occurs near an elevation of -762 m. This elevation corresponds to the elevation of a pumping zone in MIU-2 and therefore the grid is finely discretized in this region and the thin fault discretization leads to an increase in the effective hydraulic conductivity of the region.

The effective hydraulic conductivity of the fault region is several orders of magnitude less than the background hydraulic conductivities of the upper fractured/sedimentary zone and the lower fractured zone (4.9×10^{-4} and 4.9×10^{-6} m/s, respectively). These results hold for both methods of the calculation with the fault region effective hydraulic conductivity being approximately a factor of 7 less than the effective hydraulic conductivity of the model domain.

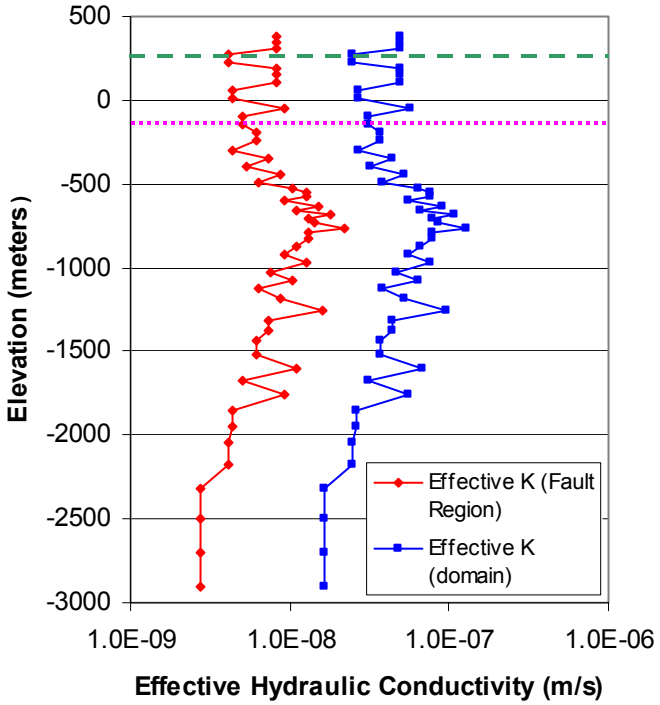

Figure 3. The effective hydraulic conductivity of the fault region (red line) and the model domain (blue line) as calculated with (3). The green and magenta horizontal lines denote the elevation of the ground surface and the upper fractured zone/sedimentary unit – lower fractured zone contact respectively.

Numerical Mesh

The study area shown in **Figure 1** is first digitized and then discretized using GMS software package. The FD discretization uses structured, orthogonal grids with variable grid spacing in all directions. **Figure 4a** presents a typical plan view of the mesh (i.e., one of the layers), where each layer (i.e., Z-direction) is comprised of 112 cells in the E-W coordinate (i.e., X-direction) and 114 cells in the N-S coordinate (i.e., Y-direction). Thus each layer consists of 12,768 FD cells. This figure also illustrates the finer grid distribution near the MIU-2 well. The minimum and maximum cell sizes in N-S direction are 10 m and 59 m, respectively. The minimum and maximum cell sizes considered in the E-W directions are 11 m and 39.8 m, respectively. Additionally, the Z-direction is divided into 55 layers with non-uniform thickness, using a minimum layer thickness of 24 m and a maximum layer thickness of 200 m (e.g., see **Figure 4b**

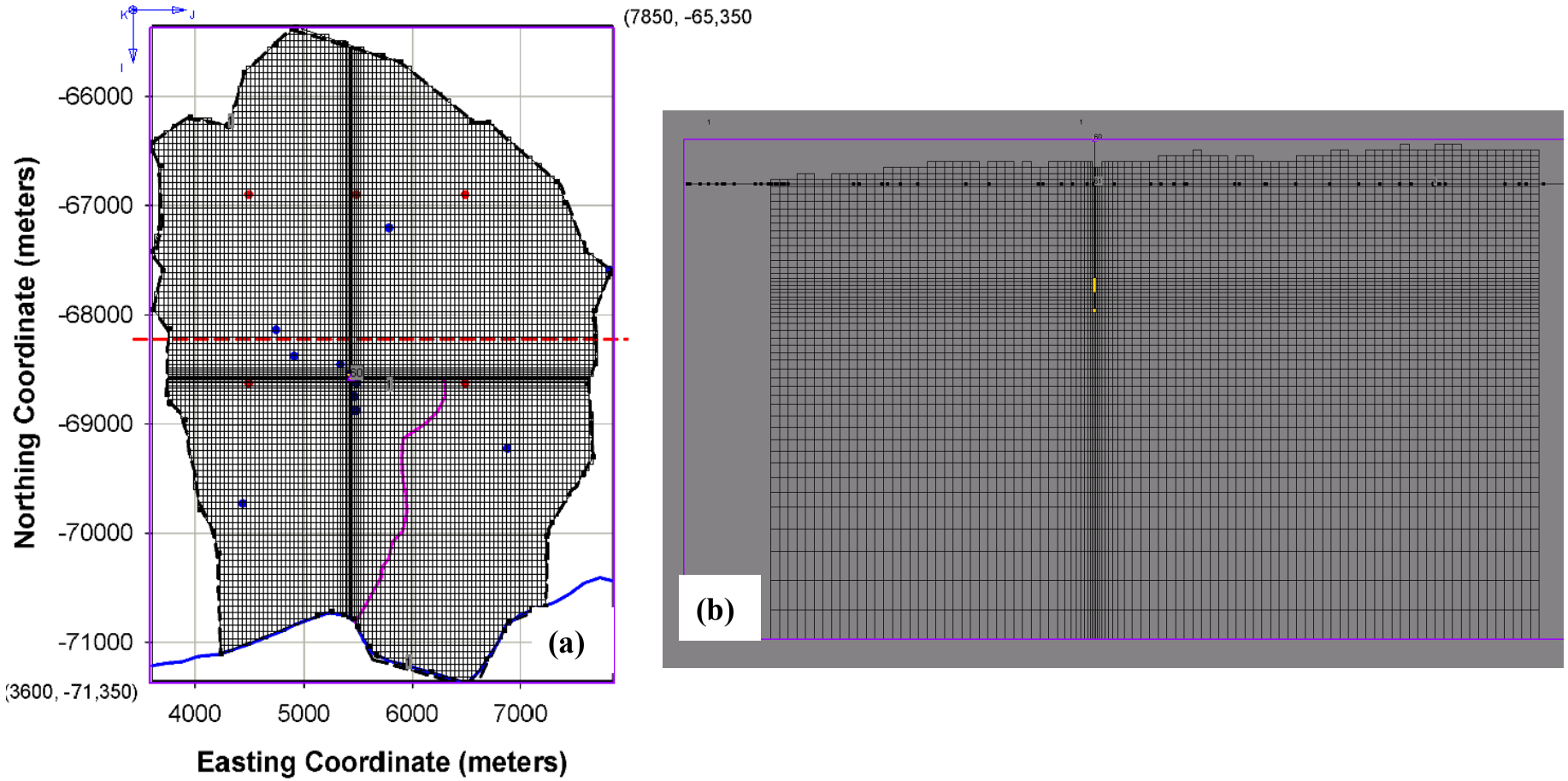

Figure 4. Representative views of the computational grid used to discretize H13 conceptual model: a) plan view in XY-plane illustrates the finer grid spacing used near and around the pumping well and b) typical transect in the YZ plane shows the variations in the topography near the surface.

for a typical transect in the YZ-plane). Finally, while the upper pumping zone includes four-25 m thick cells, the lower pumping zone involves a single 32 m thick cell. In all, the computational model consists of 702,240 cells.

Initial and Boundary Conditions

For the steady-state simulations the starting head values are simply set to be 5 m below the ground surface (i.e., the water table is -5 m below the ground surface) as was specified by JNC in the H-13 Technical Specifications. However, in order to incorporate the effect of site topography into the model, starting from the first (i.e., uppermost) layer, any cell that has an elevation greater than the ground surface, are simply considered as *inactive*. Here, the word inactive is a MODFLOW terminology and indicates that such a cell simply does not contribute to the numerical solution process. For instance, **Figure 5** illustrates a typical map of all active zones (i.e., the gridded portions of the map) for layer 4 (this layer lies between elevations 250 to 290 m). The white region indicates the inactive cells that fall above the ground surface. Additionally, **Figure 6** shows a plan view example of the fairly complex starting (i.e., initial) head field that is incorporated into the model. During the pumping phase of the simulations, the converged steady-state heads will serve as the initial condition. The top boundary condition is treated as a fixed (i.e., constant) head boundary, with no areal recharge. The three sides forming the north, east, and west sides (i.e. ridge part) boundaries are also considered to be fixed head. The head values for all constant head boundaries vary spatially and are the same as the starting head values. Finally the south side, where the Toki river flows, as well as the bottom boundary (i.e., layer 55) are set to no-flow boundaries.

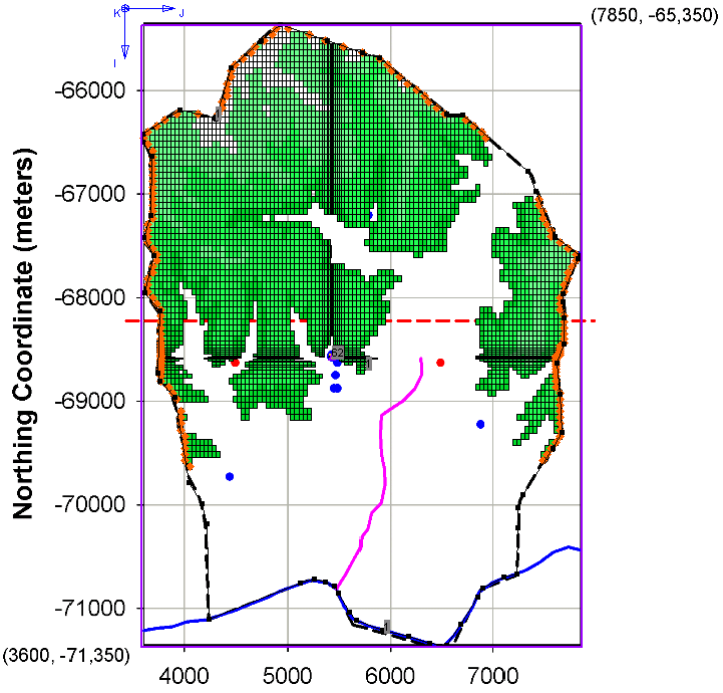

Figure 5. Plan view for layer 4 exemplifying the implementation of elevation dependent topography using MODFLOW active node option.

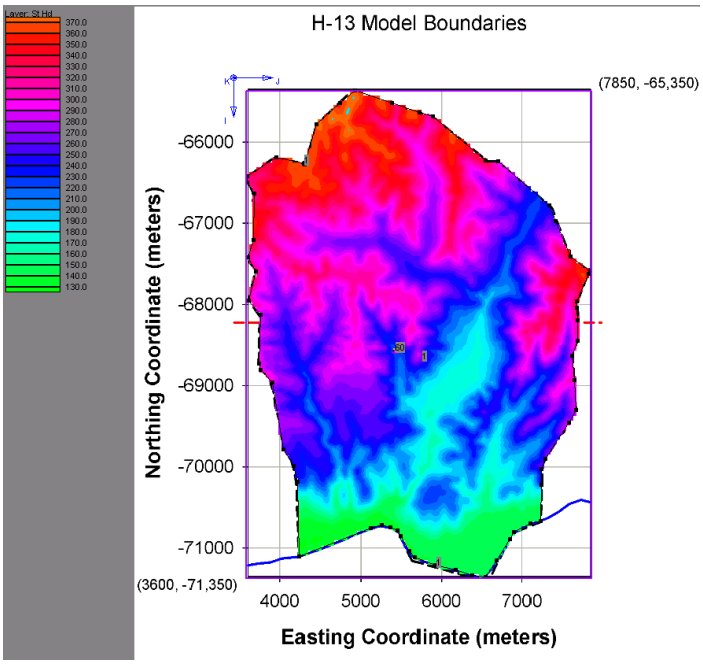

Figure 6. Typical plan view illustrating initial (starting) head field for the H13 model

Results of Steady-State and Transient Simulations

Steady-state Simulations

Figure 7 illustrates the calculated steady-state head contours along the Y-Z transect at X=5,433.3 (m) (i.e., near the pumping well locations). As a contrast, the hydraulic conductivity field is also plotted in the background. It is clear that the fault (i.e., the regional effect) has a great influence on the head field distribution. However, the local topography, especially closer to the surface, tends to dominate the shape of the head contours. In fact, the contours near the surface are similar to those discussed by Freeze and Cherry (1979, pg. 195), where a series of small independent flow cells are present. It is also important to note that, although we do not explicitly consider recharge in this simulation, imposition of elevation dependent head boundary condition is akin to creating an implicit recharge along the base of the higher conductivity unit. That is because the gradient in head near the surface results in a flux into the system. This point will become clearer when we discuss the particle tracking results. However, when the boundary condition for the upper boundary is changed to the no flow condition (still without any recharge), the head contours, away from the fault, across the lower and upper units show little to no gradient. For example, **Figure 8** shows the head field, for the same YZ-plane as in **Figure 7**, except the top boundary is now a no flow condition. Even though the fault still plays a significant role, the shape of the contours near the surface is no longer controlled by the regional topography and the head gradient across the high and low *K* units is negligible.

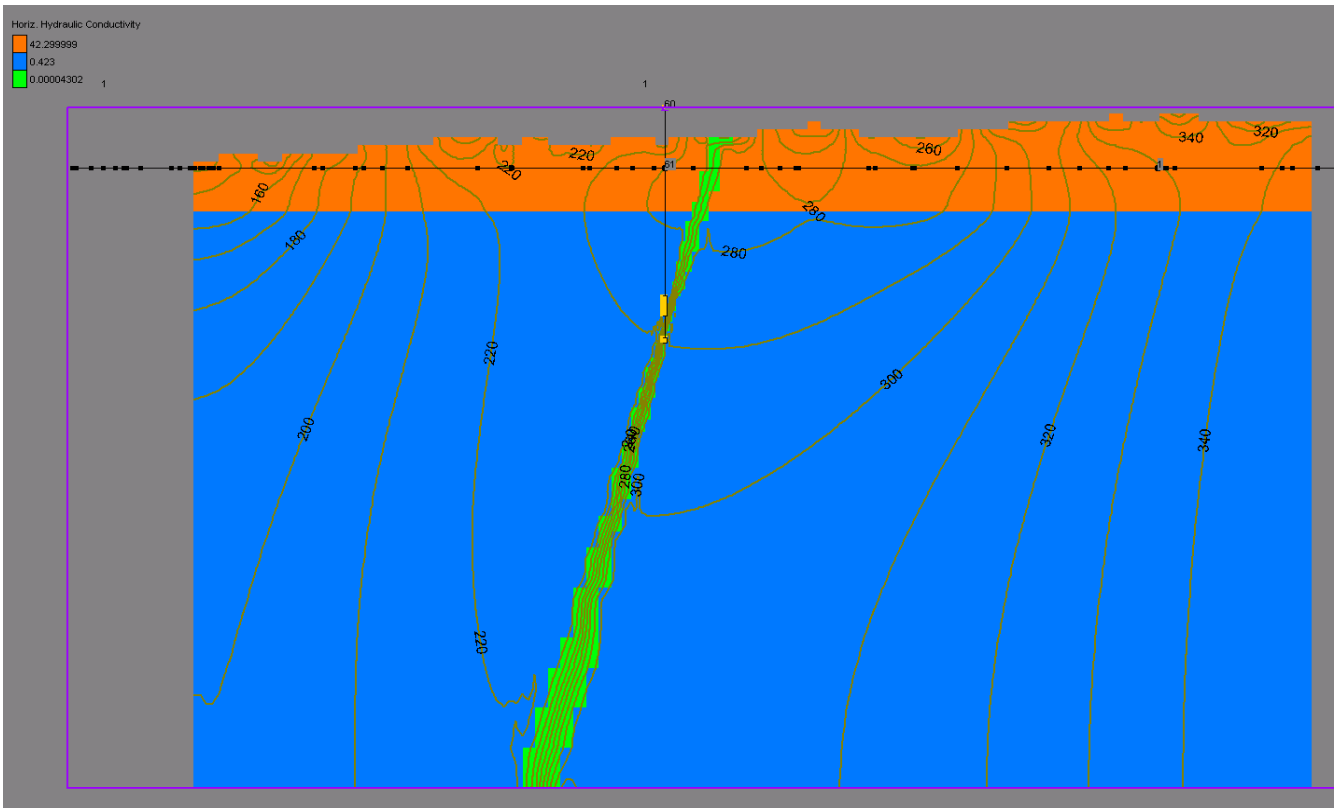

Figure 7. Computed steady-state head field in the YZ transect near the pumping well locations using fixed head surface boundary condition.

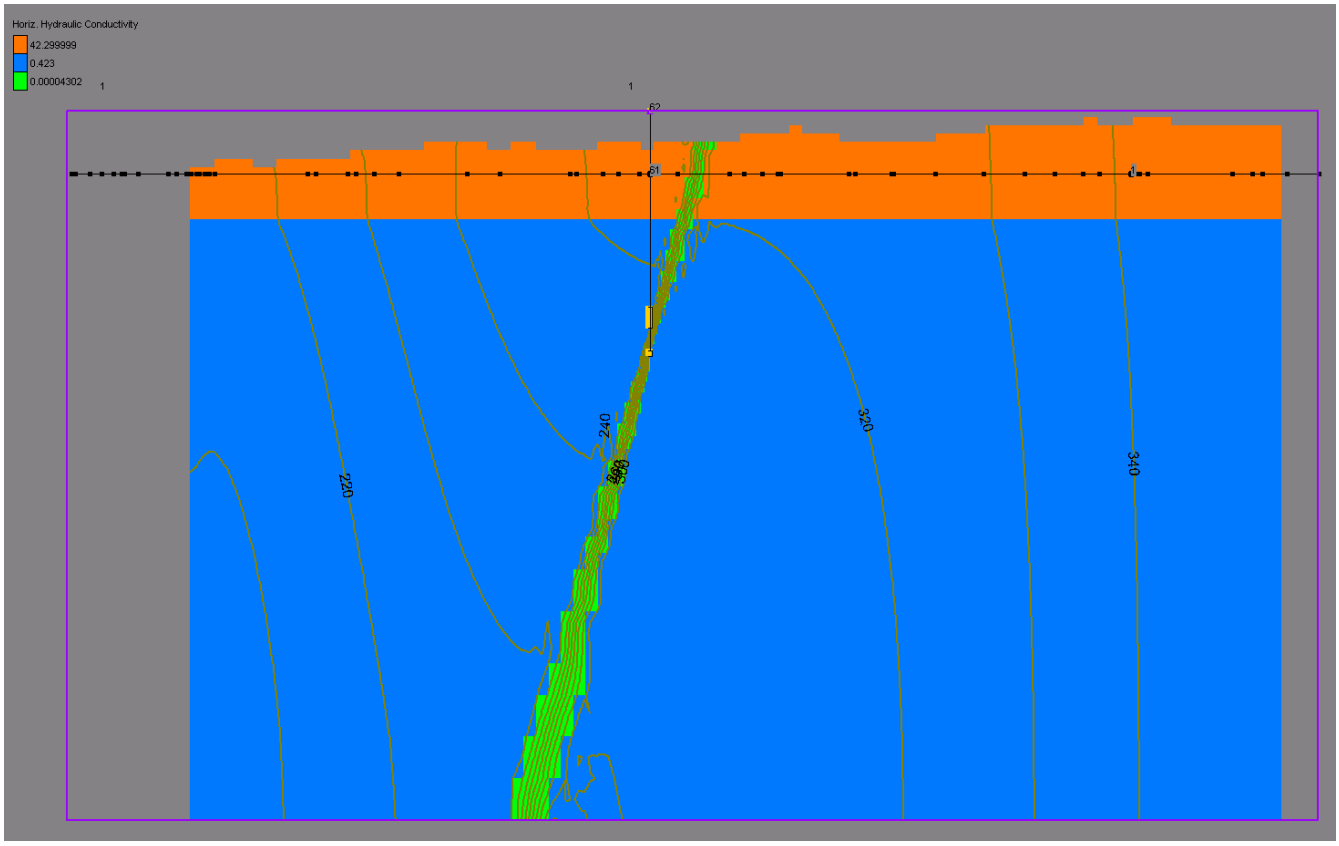

Figure 8. Computed steady-state head field in the YZ transect near the pumping well locations using no flow surface boundary condition.

The cell-to-cell fluxes (i.e., Darcy velocity) vectors can also be used to illustrate the differences between the choice of constant head and no-flow top boundary condition. **Figure 9** shows the vector plots for the constant head (**Figure 9a**) and no-flow (**Figure 9b**) boundary conditions, for the same YZ-plane as in **Figures 7** and **8**. While for both types of boundary conditions the fluxes in the lower unit and the fault are negligibly small, the fluxes within the upper unit (i.e., the high *K* zone) are significantly larger. The vectors in **Figure 9a** basically follow the same trend as their corresponding head contours, i.e., where at the base of high *K* zone the vectors run parallel along the base, and clearly show the local discharge and recharge zones. However, the vectors in **Figure 9b** are much smaller than those in **Figure 9a**, even at the base of the high *K* unit, indicating again there is no implicit recharge when the top boundary condition is no-flow. Next, we calculated several statistical measures of the volumetric fluxes. These include the minimum, maximum, mean, and standard deviation of the fluxes for all FD nodes. The arithmetic mean of the absolute value of the net volumetric flux (i.e., sum of the fluxes in and out of each face of the volume surrounding a node) is ~0.01 m^3/sec and the sample standard deviation is found to be ~0.038 m^3/sec. Additionally, the maximum net volumetric flux of 1.14 m^3/sec (which actually has a negative sign) occurs at the upper unit in the coordinates X=6,523.7 m, Y=-65,971 m, and Z=190 m. The minimum net flux of zero is found to be along the bottom no-flow boundary (note that, there are many control volumes with zero flux in the lower geological unit).

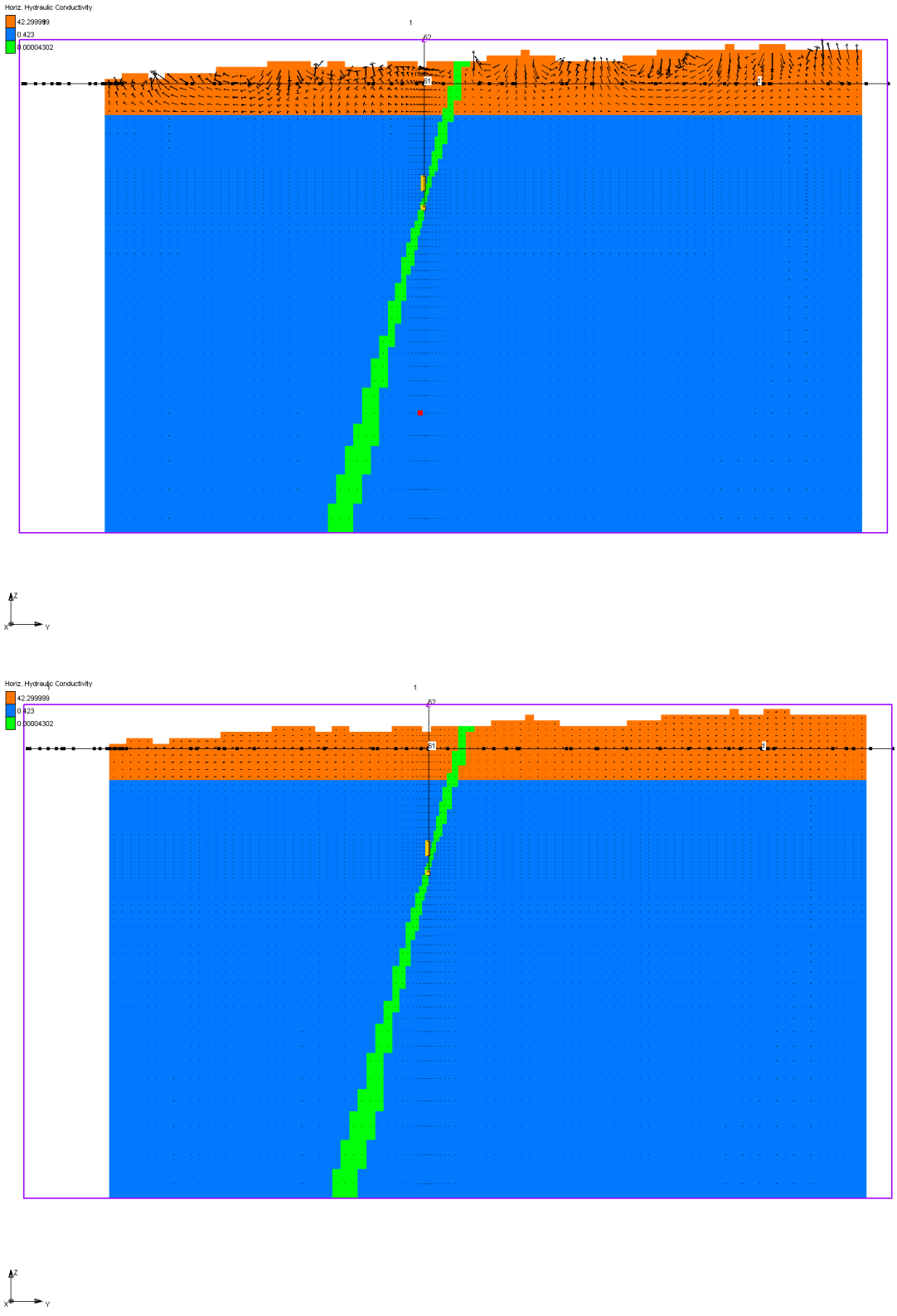

(a)

(b)

Figure 9. Darcy flux vectors for the same location as Figures 7 and 8, illustrating the effect of: a) fixed head top boundary condition and b) no flow top boundary condition.

Surface Boundary Fluxes

The amount of flux into and out of the model along the top surface boundary of the domain has been calculated for the steady-state case. The fluxes are summarized in **Table 2**. The surface flux values are calculated as negative for flux into the model and positive for flux out of the model. **Table 2** shows that there is slightly more flow into the model than out - a difference of 0.093 m/sec. The majority of the flux calculations are centered around zero with a median value of –5.45E-10 m/sec, or nearly zero. The flux distribution is skewed to the negative (inflow) side with a mean of –1.01E-05 m/sec.

Table 2. Summary of model surface fluxes**.**

Parameter	**Value (m/sec)**
Minimum	-1.21E-03
Maximum	5.56E-04
Mean	-1.01E-05
Median	-5.45E-10
Sum of Model Input	-0.384
Sum of Model Output	0.291

The spatial locations of the flux in and out of the model are shown in **Figure 10**. Flow into the model, negative values shown by the blue colors, occurs mainly along the edges of the river valleys and in the higher elevations. The brown colors in **Figure 10** indicate areas of model discharge. These areas are generally in the southern portion of the model, along the Toki River, and along the smaller drainages in the model, such as the southern reaches of the Hiyoshi River. There is not a simple correlation between elevation and recharge. This complex relationship is due to the varying hydraulic conductivity values in the model and localized flow cells within the model caused by the local topographic highs and lows. These factors create dischasrge zones that are a combination of local flow cells and more regional groundwater flow. Additionally, the relationship between the elevation and the recharge or discharge is complicated by the coarse vertical discretization of the model.

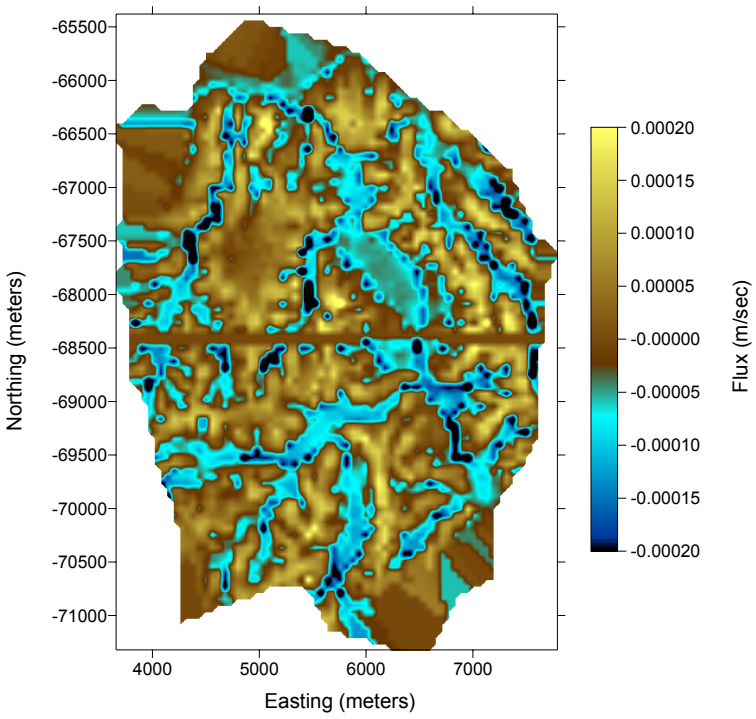

Figure 10. Map of fluxes at the upper surface of the model. Negative values indicate flux into the model and positive values indicate flux out of the model.

Particle Tracking for Baseline Steady-state Case

To evaluate the groundwater flow paths, particle tracking was performed for 24 particles, which were released from predetermined locations. **Table 3** lists the starting coordinates assigned by JNC for each particle along with model coordinates, the corresponding geological unit, hydraulic conductivity, and porosity. The model coordinates were chosen to be as close as possible to the JNC assigned values. Typical steady-state particle tracks, at the same transect as **Figure 7**, are shown in **Figure 11**. Also, to contrast the particles travel path with the steady-state head values, head contours are also included in the background. As the figure depicts, particles released from the north side of the fault (i.e., the left side in the figure), immediately move up toward the surface. This is also the case for most particles released from the fault's south side, with the exception of two particles that tend to move downward and then exit the model at the southern boundary. Another interesting feature of this figure is the horizontal flow that occurs at the base of the high *K* layer. This is another way of illustrating of the previously described implicit recharge that arises from imposing constant head on the top boundary. Although not immediately obvious, particles generally discharge into zones with lower simulated head values, such as the Hiyoshi and Toki rivers, and this is the case for both the upper and lower units.

Table 3. JNC assigned and model particle locations used to evaluate flow paths behavior

Particle	JNC Coordinates			Model coordinates			Geol.	*K*	ϕ
No.	*X* (m)	*Y* (m)	*Z* (m)	*X* (m)	*Y* (m)	*Z* (m)	Unit	(m/s)	(-)
1	4488.83	-66900	-250	4496.40	66912.34	-245	lower	4.90E-06	0.01
2	5488.83	-66900	-250	5492.32	66912.34	-245	lower	4.90E-06	0.01
3	6488.83	-66900	-250	6484.08	66912.34	-245	lower	4.90E-06	0.01
4	4488.83	-66900	-500	4496.40	66912.34	-490	lower	4.90E-06	0.01
5	5488.83	-66900	-500	5492.32	66912.34	-490	lower	4.90E-06	0.01
6	6488.83	-66900	-500	6484.08	66912.34	-490	lower	4.90E-06	0.01
7	4488.83	-66900	-750	4496.40	66912.34	-762	lower	4.90E-06	0.01
8	5488.83	-66900	-750	5492.32	66912.34	-762	lower	4.90E-06	0.01
9	6488.83	-66900	-750	6484.08	66912.34	-762	lower	4.90E-06	0.01
10	4488.83	-66900	-1000	4496.40	66912.34	-1025	lower	4.90E-06	0.01
11	5488.83	-66900	-1000	5492.32	66912.34	-1025	lower	4.90E-06	0.01
12	6488.83	-66900	-1000	6484.08	66912.34	-1025	lower	4.90E-06	0.01
13	4488.83	-68629.36	-250	4496.40	68634.25	-245	lower	4.90E-06	0.01
14	5488.83	-68629.36	-250	5492.32	68634.25	-245	lower	4.90E-06	0.01
15	6488.83	-68629.36	-250	6484.08	68634.25	-245	lower	4.90E-06	0.01
16	4488.83	-68629.36	-500	4496.40	68634.25	-490	lower	4.90E-06	0.01
17	5488.83	-68629.36	-500	5492.32	68634.25	-490	lower	4.90E-06	0.01
18	6488.83	-68629.36	-500	6484.08	68634.25	-490	lower	4.90E-06	0.01
19	4488.83	-68629.36	-750	4496.40	68634.25	-762	lower	4.90E-06	0.01
20	5488.83	-68629.36	-750	5492.32	68634.25	-762	lower	4.90E-06	0.01
21	6488.83	-68629.36	-750	6484.08	68634.25	-762	lower	4.90E-06	0.01
22	4488.83	-68629.36	-1000	4496.40	68634.25	-1025	lower	4.90E-06	0.01
23	5488.83	-68629.36	-1000	5492.32	68634.25	-1025	lower	4.90E-06	0.01
24	6488.83	-68629.36	-1000	6484.08	68634.25	-1025	lower	4.90E-06	0.01

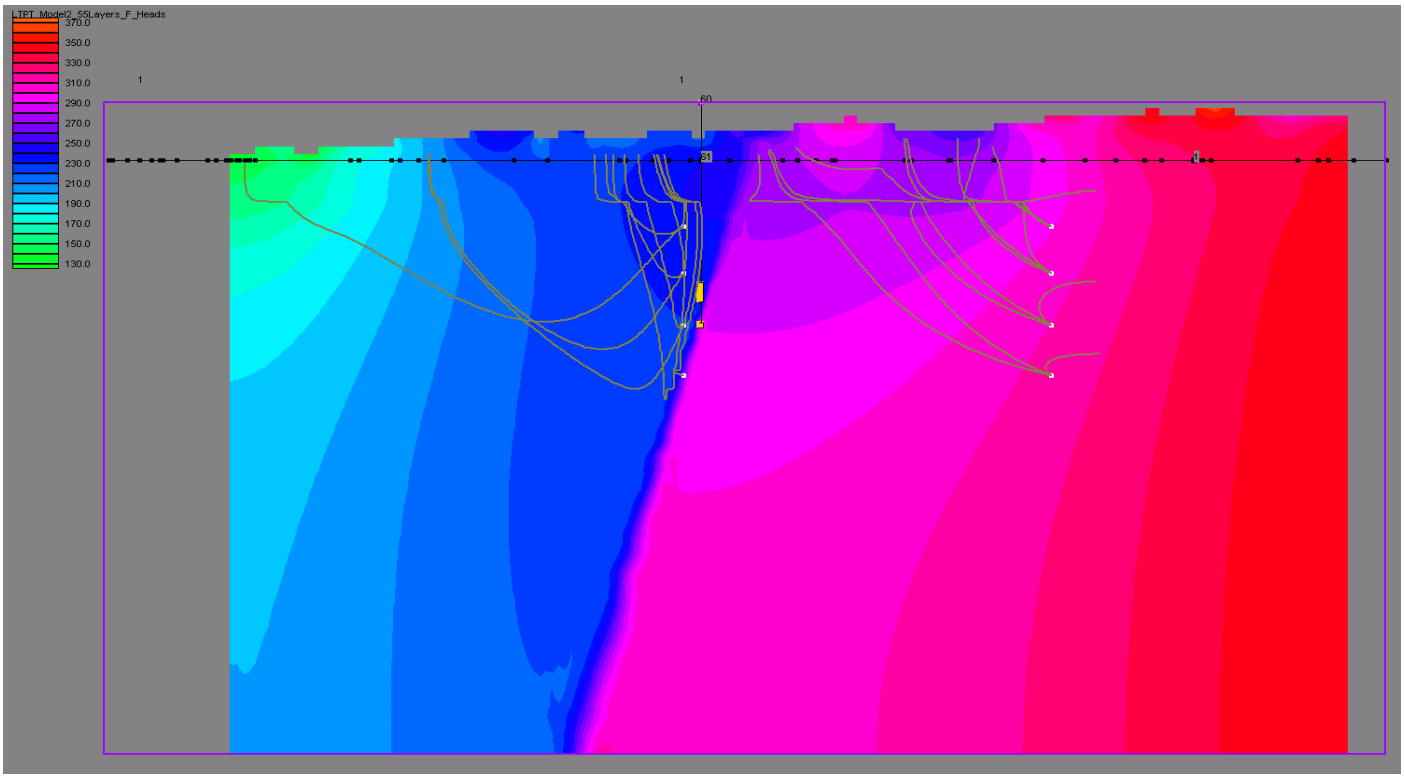

Figure 11. Path lines for the steady-state particle tracks for the same transect as Figure 7, with the steady-state head values also plotted in the background. In general, particles released from both sides of the fault move up toward the surface. The horizontal flow occurring at the base of the high *K* layer also shows the implicit recharge arising from imposing constant head on the top boundary.

Table 4 lists complete path traversed by each particle (i.e., the coordinates in the XYZ directions), along with the corresponding FD node, the travel distance, travel time, and Darcy velocities. To graphically represent the particle path lines discussed in this table, **Figure 12** shows three-dimensional views of the particle tracks. The color scale in the upper image indicates the log10 travel time in years and clearly shows the distinction between long travel times for particles released south of the fault and for shorter travel times for the particles release on the north side of the fault. The color-scale in the middle image of shows the log_{10} Darcy velocity in m/s along each path. This image shows that up to two orders of magnitude variation in Darcy velocity can occur along a single pathway. The color scale in the bottom image indicates the log_{10} pore velocity in m/s and shows the changes in velocity due to the porosity differences in the different geologic layers. Finally, **Figure 13** summarizes the total travel length and Darcy time as a function of particle number. Note that while particle 13 (located at top, north, left) travels the longest distance (i.e., 3232 m), particle 15 only travels 501 m and thus has the minimum travel distance. Particle 15 also has the shortest travel time of 3.57×10^{7} sec while particle 22 has the longest travel time of 4.38×10^{10} sec.

Table 4. Path lines for the 24 particles listed in Table 3. In addition to the path lines coordinates, the travel distance, travel time, Darcy velocities, and the average porosity values are also included.

Particle Number	X (m)	Y (m)	Z (m)	Travel Length (m)	Travel Time (yrs)	Darcy Velocity (m/sec)	Velocity (m/sec)	Average Porosity
1	5.293E+03	-6.725E+04	2.100E+02	1.19E+03	4.44E-01	6.90E-06	8.46E-05	0.08
2	5.716E+03	-6.759E+04	2.100E+02	9.83E+02	3.83E-01	6.43E-06	8.13E-05	0.08
3	6.928E+03	-6.719E+04	1.700E+02	7.95E+02	4.43E-01	3.32E-06	5.68E-05	0.06
4	5.430E+03	-6.735E+04	2.100E+02	1.47E+03	1.05E+00	2.84E-06	4.43E-05	0.06
5	6.391E+03	-6.811E+04	1.700E+02	1.80E+03	9.40E-01	4.30E-06	6.06E-05	0.07
6	7.198E+03	-6.671E+04	-6.226E+01	1.08E+03	8.88E-01	1.83E-06	3.85E-05	0.05
7	5.755E+03	-6.760E+04	2.100E+02	2.07E+03	2.72E+00	1.20E-06	2.41E-05	0.05
8	6.464E+03	-6.824E+04	1.567E+02	2.08E+03	1.64E+00	2.21E-06	4.02E-05	0.06
9	7.177E+03	-6.671E+04	-5.337E+02	8.26E+02	1.03E+00	2.54E-07	2.54E-05	0.01
10	6.435E+03	-6.828E+04	1.300E+02	3.13E+03	4.40E+00	1.10E-06	2.25E-05	0.05
11	6.456E+03	-6.824E+04	1.403E+02	2.15E+03	2.43E+00	1.02E-06	2.80E-05	0.04
12	7.177E+03	-6.669E+04	-9.125E+02	7.74E+02	8.50E-01	2.89E-07	2.89E-05	0.01
13	5.270E+03	-7.069E+04	8.000E+01	3.23E+03	5.67E+00	4.41E-07	1.81E-05	0.02
14	6.065E+03	-6.905E+04	1.300E+02	1.01E+03	7.14E-01	1.97E-06	4.47E-05	0.04
15	6.300E+03	-6.876E+04	1.300E+02	5.01E+02	1.81E-01	6.59E-06	8.78E-05	0.08
16	5.851E+03	-6.982E+04	1.300E+02	2.69E+03	5.58E+00	2.56E-07	1.53E-05	0.02
17	6.117E+03	-6.900E+04	1.300E+02	1.17E+03	1.39E+00	7.88E-07	2.65E-05	0.03
18	6.286E+03	-6.878E+04	1.300E+02	7.35E+02	5.25E-01	1.64E-06	4.44E-05	0.04
19	5.850E+03	-6.983E+04	1.300E+02	2.96E+03	7.87E+00	2.11E-07	1.19E-05	0.02
20	6.198E+03	-6.891E+04	1.300E+02	1.40E+03	2.76E+00	3.88E-07	1.61E-05	0.02
21	6.300E+03	-6.876E+04	1.300E+02	1.09E+03	1.29E+00	1.07E-06	2.67E-05	0.04
22	6.152E+03	-6.896E+04	1.300E+02	2.75E+03	3.59E+01	4.35E-08	2.43E-06	0.02
23	6.241E+03	-6.885E+04	1.300E+02	1.72E+03	2.12E+01	6.44E-08	2.57E-06	0.03
24	6.308E+03	-6.872E+04	1.300E+02	1.70E+03	2.22E+01	7.30E-08	2.43E-06	0.03

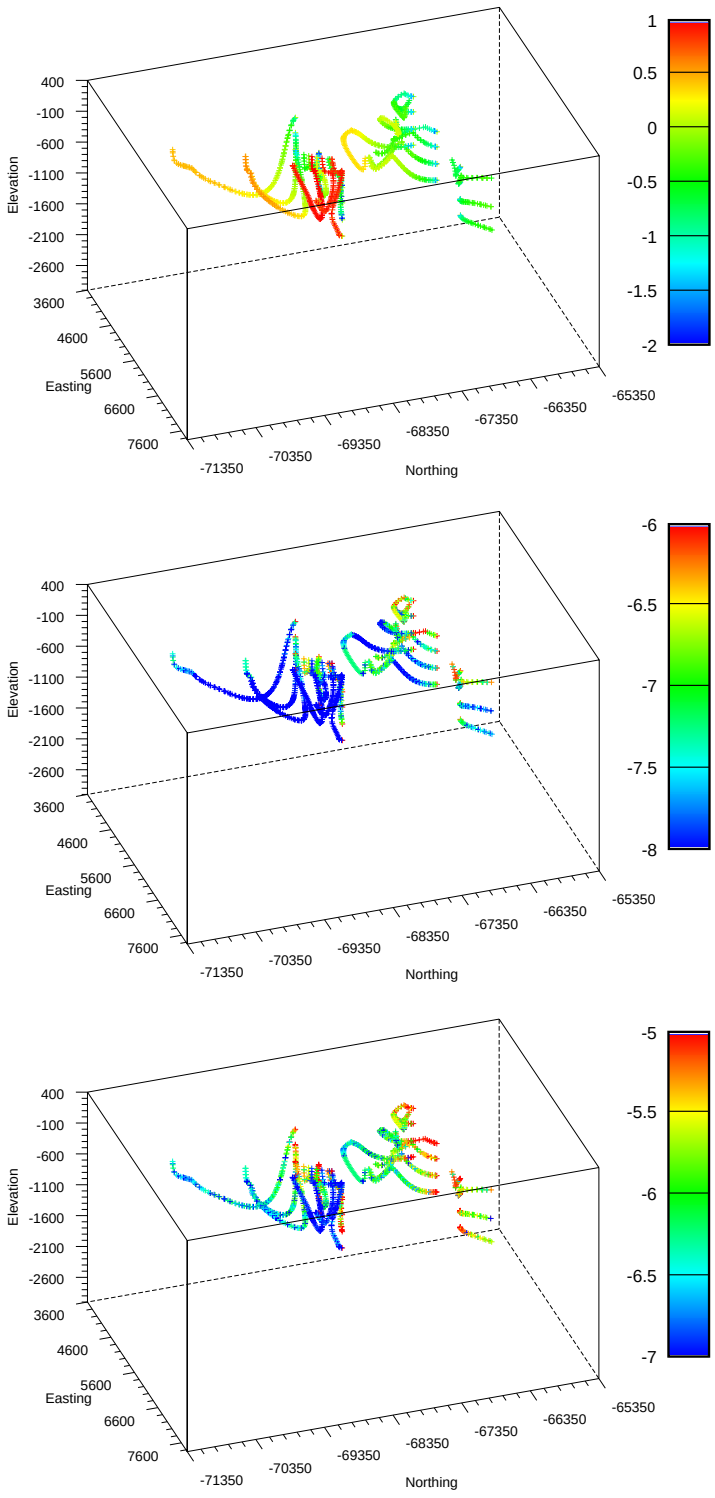

Figure 12. 3-D images of the particle tracks under steady-state conditions. The color scale indicates log10 travel time in years (upper image), log10 Darcy velocity in m/sec (middle image) and log10 pore velocity in m/sec (lower image).

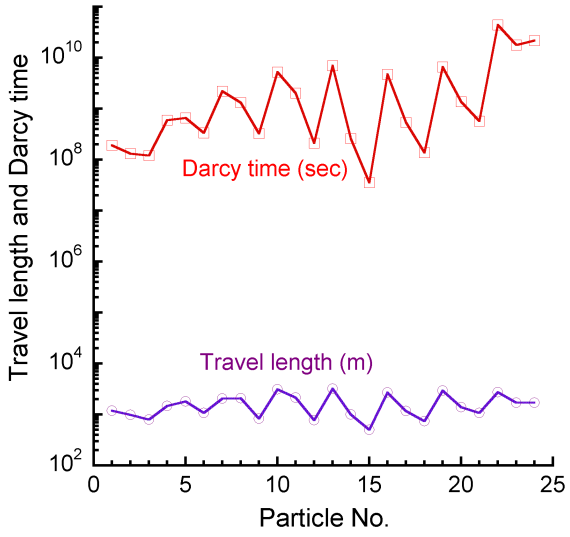

Figure 13. Total travel length and Darcy time versus particle number for the steady-state simulation.

Long-term Pumping Test Simulations

Next, we extend the steady-state simulations and consider the groundwater response due to pumping. To do this, the pumping rate of each well is set to a constant value of 20 L/min (i.e., 28.8 m^3/day). The wells are pumped for a period of 14 days, followed by an additional 36 days of recovery, making the total stress period to be 50 days. Also, to isolate the influences of the pumping above and below the fault, separate simulations are conducted. For the pumping above the fault, the flux is equally distributed across the four FD cells in the pumping zone (i.e., 7.2 m^3/day/cell). However, since for the pumping below the fault there is only one FD cell, the entire pumping rate of 28.8 m^3/day is applied to that node.

Figure 14 shows the head contours after 14 days of pumping the upper well in the YZ-plane crossing the wells. Comparing this figure to **Figure 7** (i.e., the head contours for the steady-state solution), we see little to no difference between the two results. This indicates that this pumping rate influences the groundwater response only slightly. This is interesting, because the near proximity of the pumping wells to the fault should result in significant contribution to the drawdown around the fault. However, the drawdown contours, presented in **Figure 15** along the same YZ-plane, illustrate a maximum drawdown of ~6 cm around the well location. Even though the zone of influence covers several hundred meters, the drawdown quickly becomes negligible away from the wells. Moreover, the drawdown response is not too different when the pumping well below the fault is considered. **Figure 16** presents the drawdown contours at three

different planes (i.e., YZ, XZ, and XY), after 14 days of pumping the lower well. As in the case pumping the upper well, the highest drawdown is confined to a zone near or at the well location, even though the maximum drawdown in this case is ~2.5 m. To better represent the drawdown behavior, at the two well locations, next we discuss the temporal variations of drawdown for these two cases as well as several other cases. However, we must first correct the calculated drawdown values for the actual wellbore diameters.

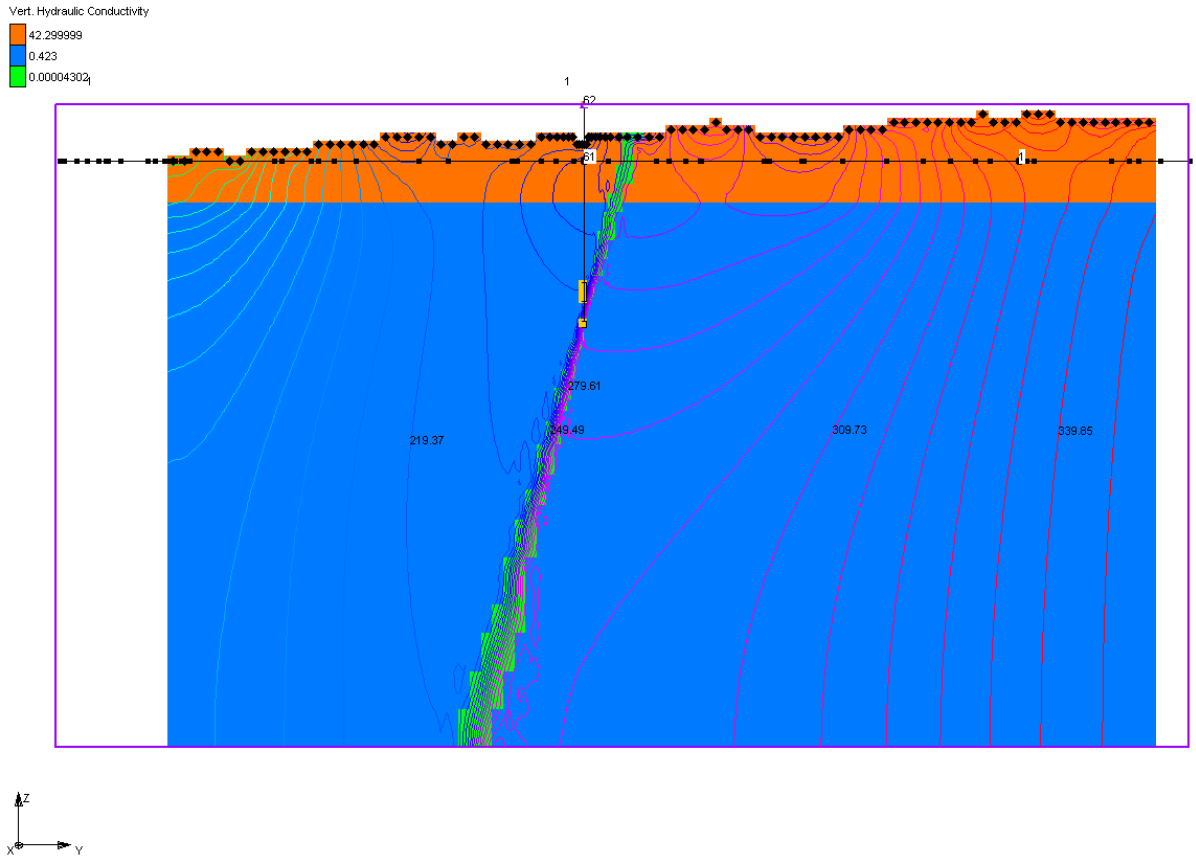

Figure 14. Contour lines for the head field after 14 days of pumping the well above the fault, with the hydraulic conductivity for the three geological units included in the background. Contrasting these results with the steady-state results (i.e., Figure 7), pumping appears to minimally impact the groundwater response.

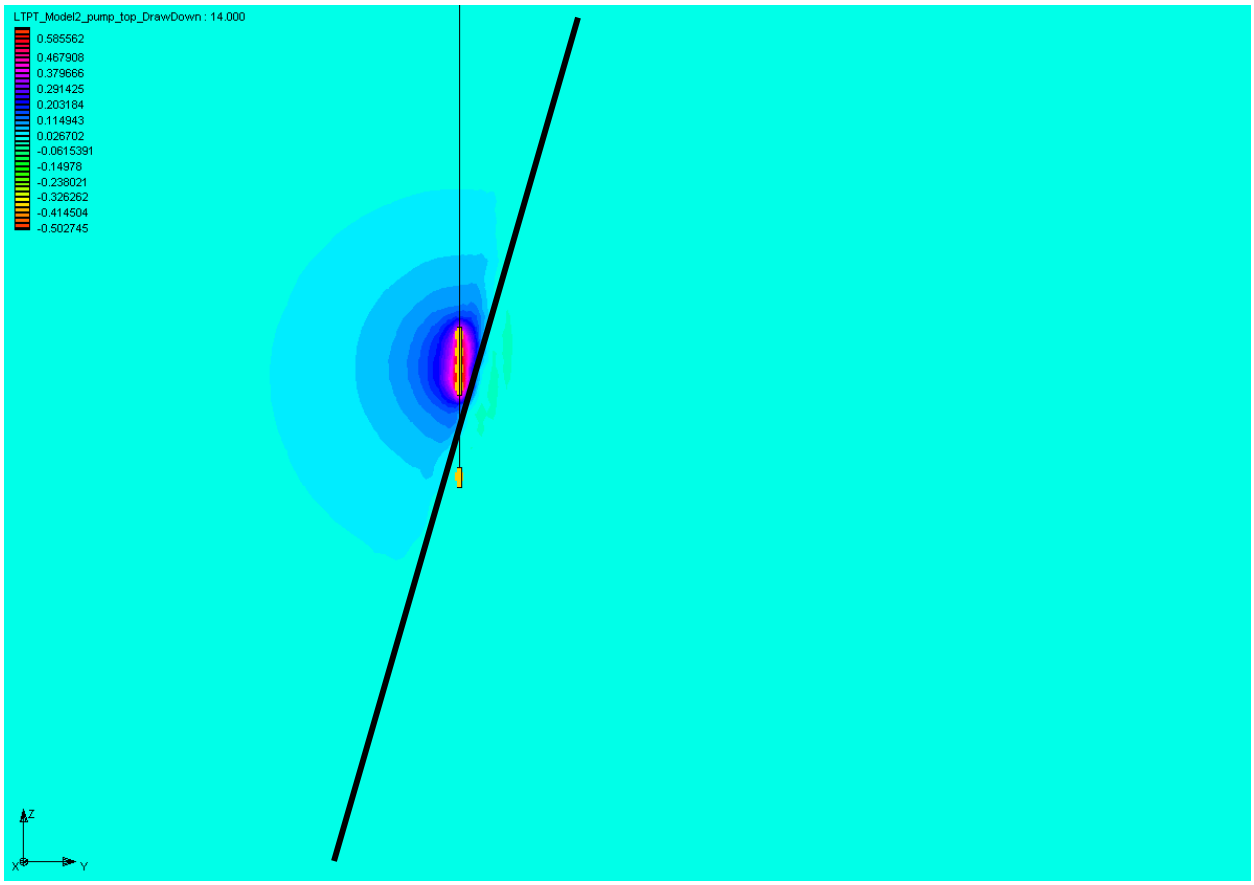

Figure 15. Close-up view of the drawdown contours for the results discussed in Figure 14, illustrate the maximum drawdown (red color) is ~6 cm. Black line shows approximate location of Tsukioshi fault.

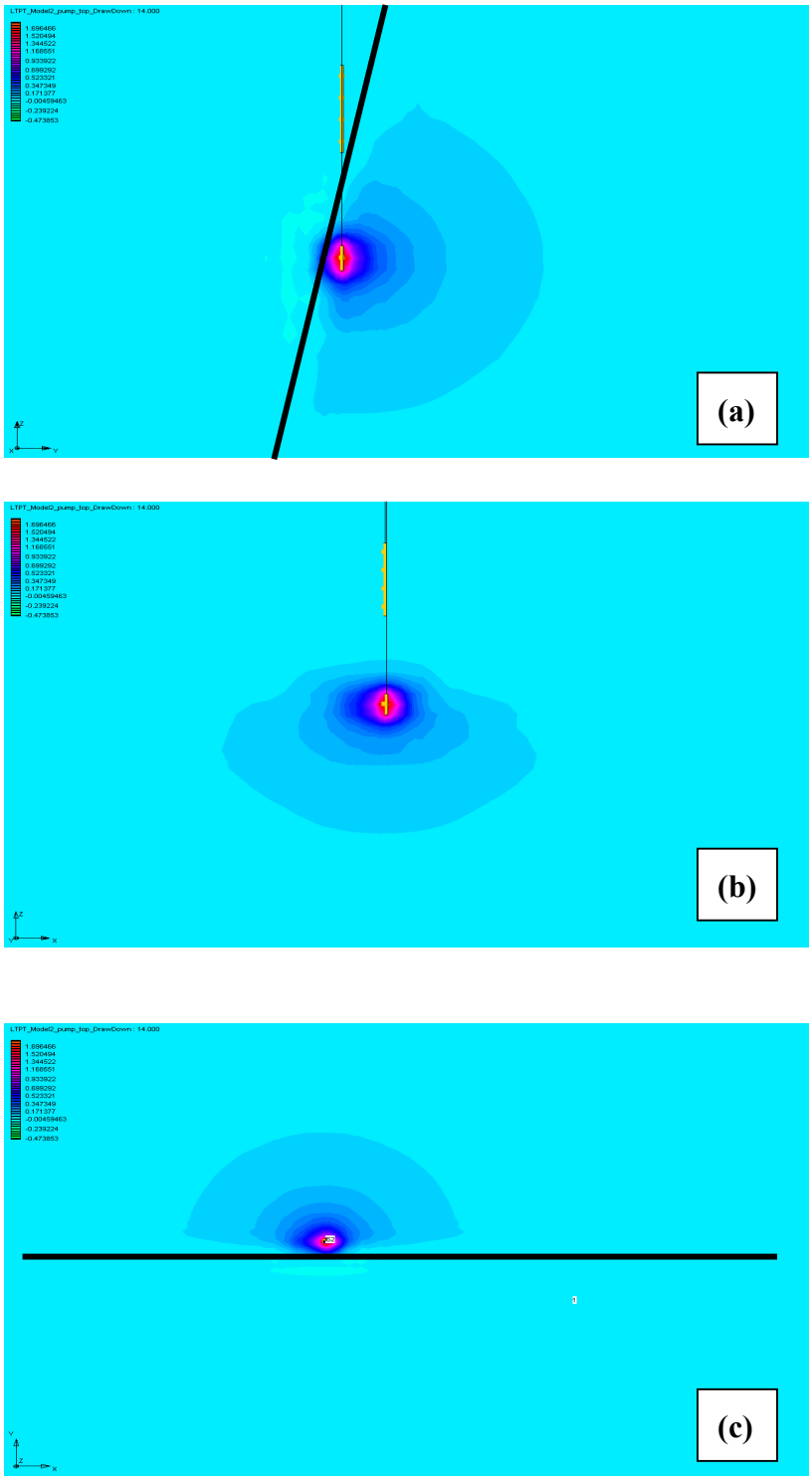

Figure 16. Close-up views of the drawdown contours after 14 days of pumping the lower well in: a) the YZ-plane, b) XZ-plane, and c) XY-plane indicate a maximum drawdown of ~2.5 m. The influence of the fault can be clearly seen in the YZ and XY transect. The black line shows the approximate location of the Tsukioshi Fault in the upper and lower images.

Wellbore correction

In numerical groundwater simulations, the grid blocks where wells are located are generally larger than the physical borehole diameter. Since it is seldom practical to resolve the grid fine enough to have the same size as the physical well diameter, wellbore corrections are often applied to the wellbore grid blocks (e.g., see Prichett and Garg, 1980). Anderson and Woessner (1992, pg. 148) suggest the following to correct the calculated head values at the well locations:

$$h_w = h_{i,j,k} - \frac{Q_{WT}}{2\pi KH} \ln\left(\frac{r_e}{r_w}\right) \tag{4}$$

where h_w and $h_{i,j,k}$ (m) respectively refer to the corrected and computed (i.e., at node *i, j, k*) head values, Q_{WT} (m^3/day) is the total pumping rate, K (m/day) is the conductivity, H (m) is the thickness of the layer where the well resides, r_e (m) is the effective well block radius, and r_w (m) is the physical well radius. For uniform grid spacing (as is our case at the well locations), Anderson and Woessner (1992, pg. 149) derive a simple form for the effective radius as:

$$r_e = 0.208a \tag{5}$$

here $a=\Delta x=\Delta y$ (m) is the grid spacing in the x and y directions. Prichett and Garg (1980) also present other relationships for r_e when the grid spacing is not uniform. Here, we set r_w=0.05 m and since both pumping wells are in the same lower geological unit, we let K=0.423 m/day (i.e., $4.9\text{x}10^{-6}$ m/sec), a=10 m (i.e., r_e=2.08 m). The layer thickness, H, is 25 m and 26 m, respectively, for the well above and below the fault. As previously noted, the pumping rate, Q_{WT}, is 28.8 m^3/day. However, when applying (4) to the well above the fault, we set Q_{WT}=7.2 m^3/day, as there are four nodes representing that well zone.

Drawdown as a measure of groundwater performance

Figure 17 shows the corrected drawdown, using (4) and (5), versus time for the two pumping locations. For both pumping zones the end of pumping period is distinctly visible since following that period the drawdown sharply drops to low drawdown values, indicating the groundwater system immediately recovers. We can notice the maximum drawdown below the fault, is generally higher than each of the well screens above the fault, although adding the drawdown for the four screens above yields roughly the same drawdown as below the fault. However, given the small drawdown values (generally several meters), pumping does not appear to severely stress the groundwater system.

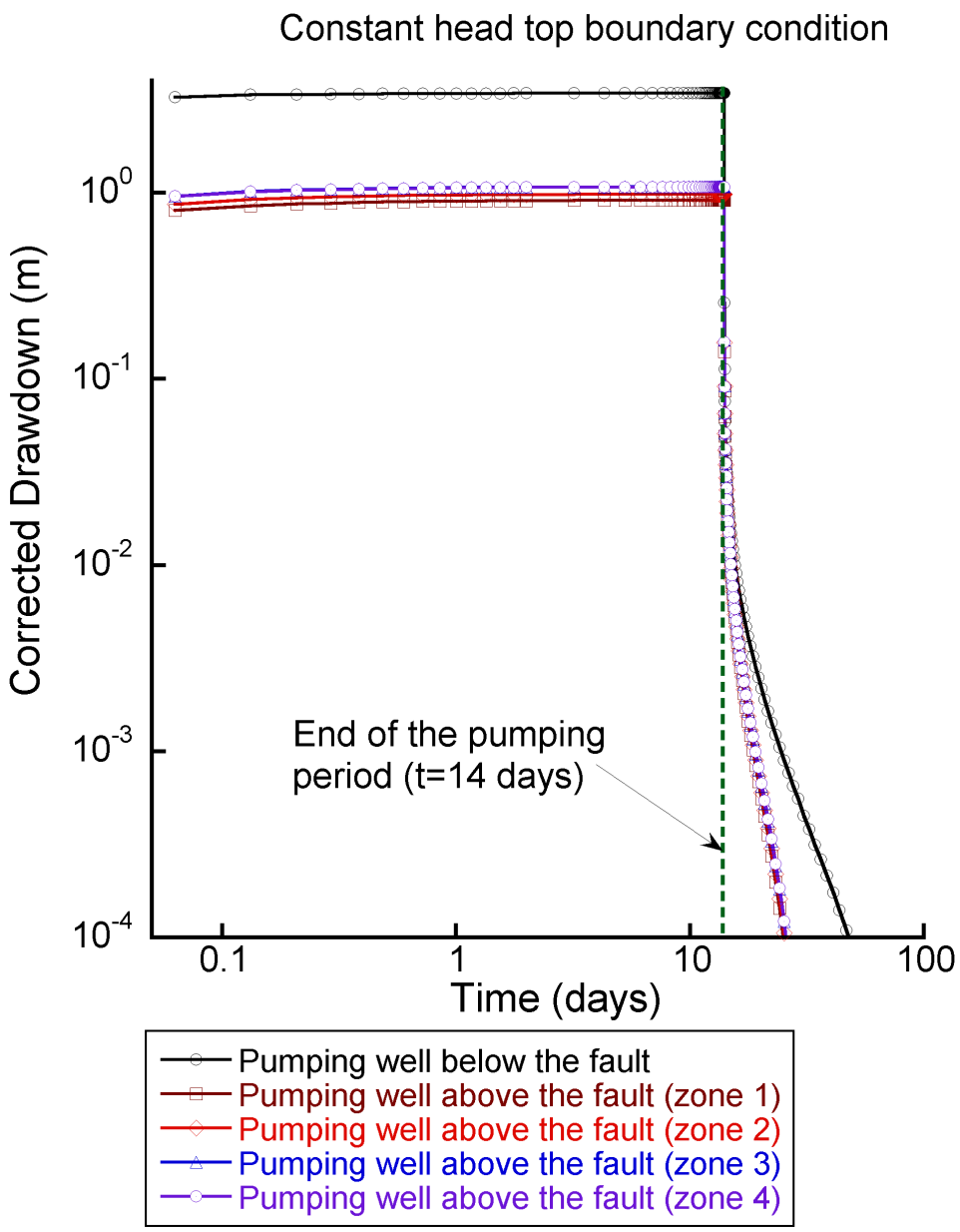

Figure 17. Corrected drawdown versus time, using fixed head top boundary condition, for the single well zone below and the four well zones above the fault. While the well zone above the fault yields a maximum drawdown of ~3.5 m, the maximum drawdown for each of the well zones above the fault are ~1 m. The sharp drop after 14 days indicates the end of pumping period, followed by the nearly full recovery at the end of 50-day period. Note that, during the recovery phase, the well zone below the fault shows a shallower drop off in slope

Next, to evaluate the effect of the top boundary condition on the drawdown, we also consider the drawdown when the top boundary is changed to a no flow condition. The corrected drawdown, as a function of time, for these cases are shown in **Figure 18**. For the case of pumping the upper well (**Figure 18a**), when the top boundary condition is changed to a no flow and all layers are treated as *all confined* (AC), the drawdown response is identical to that of constant head boundary condition case. However, when the various layers are treated as *confined-unconfined* (CU), after 14 days the maximum drawdown is slightly larger than the AC layer type (see below for a description of layer types CU and AC). In order to test the sensitivity of the drawdown to the specific storage of the upper layer, an S_s value of 10^{-7}(1/m) was also run subject to no flow top boundary condition and using the CU layers option. These results are also shown in Figure 18. We certainly see similar behavior for the reduced S_s case, even though before the end of pumping period the reduced S_s case has higher drawdown than the other two cases considered. In addition, for the cases that use AC layers the maximum drawdown is achieved within one day, but for the other two cases the drawdown continues to increase. Yet, when pumping the lower well (**Figure 18b**), for all cases the temporal variations of drawdown appear to be roughly similar, i.e., the maximum drawdown as well as the drawdown during the recovery period. Here, the bottom line is that, pumping below the fault appears to be less sensitive to the choice of the boundary condition and aquifer type.

.

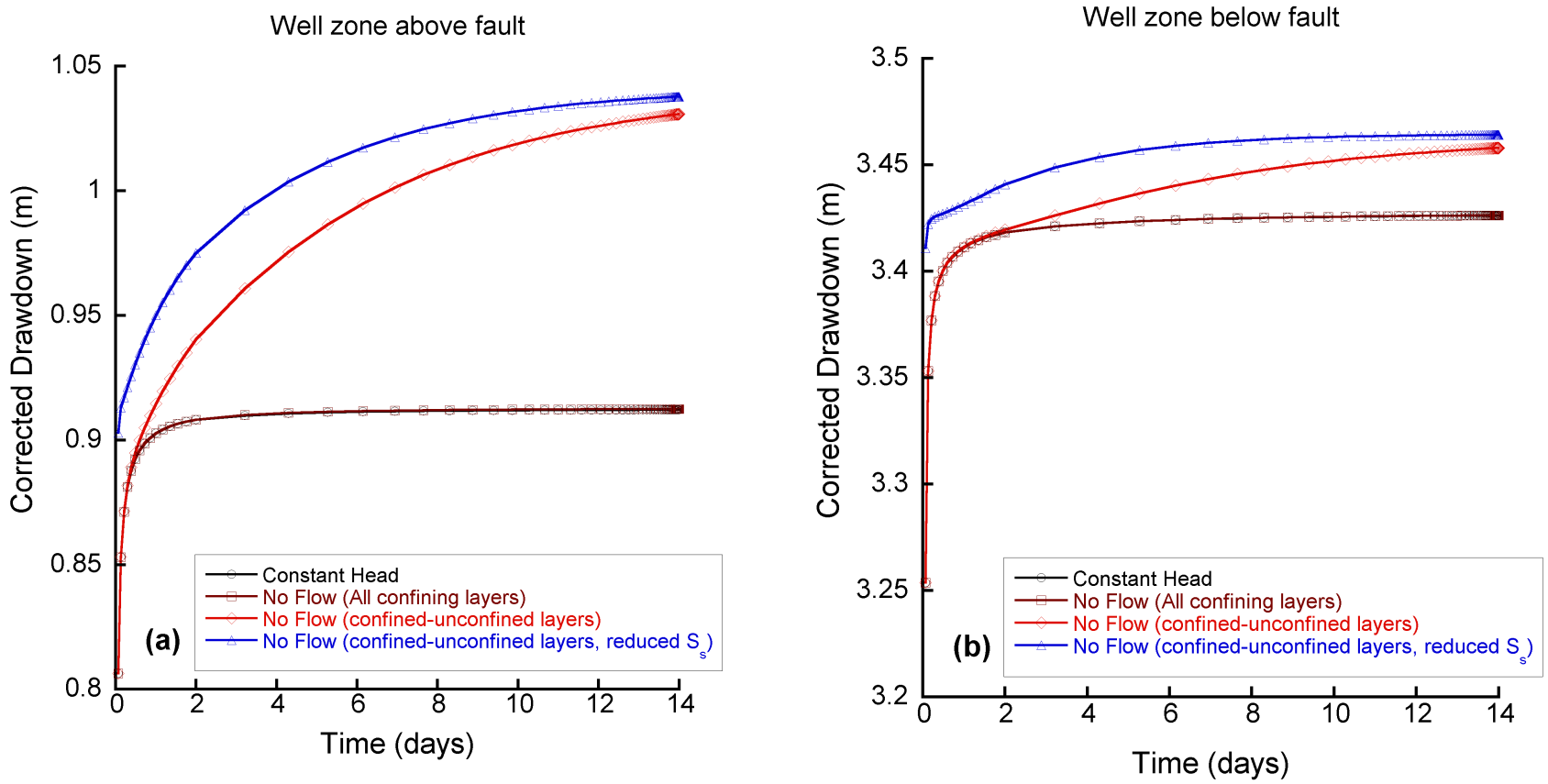

Figure 18. Corrected drawdown versus time for 14 days of pumping, illustrating the effects of top boundary condition (i.e., fixed head versus no flow), choice of layer's confinement, and reduced specific storage for: a) pumping above the fault and b) pumping zone below the fault. Note that in both figures, drawdown for constant head and no flow with all confining layers are not only identical, they also reach a constant value within ~2 days of pumping. However, the drawdown for the no flow case where the layers are treated as confined-unconfined is an increasing function of time.

Within the MODFLOW parlance, the choice of layer type (e.g., AC and/or CU stated above) is controlled through the parameter LAYCON in (see McDonald and Harbaugh, 1988; Harbaugh and Mcdonald, 1996). In general, LAYCON accounts for the manner in which the transmissivity (*T*) and storage coefficient (*S*) are treated within the model. **Table 5** summarizes the various LAYCON values in MODFLOW and their physical implications on the model.

Table 5. LAYCON parameter values in MODFLOW (Harbaugh and Mcdonald, 1996)

LAYCON	Layer Type	Explanation
0	Confined (C)	*T* and *S* are constant for the entire simulation.
1	Unconfined (U)	Layer *T* varies and *S* is constant (only valid for the first layer).
2	CU1	Layer *T* is constant and *S* may alternate between C and U values. If the layer desaturates, vertical flow from above is limited.
3	CU2	Layer *T* varies and *S* may alternate between C and U values. If the aquifer desaturates, vertical flow from above is limited.

As **Table 5** indicates the first layer is generally treated as unconfined (i.e., LAYCON=1). In this work, for both steady-state and transient simulations the first layer is always set as unconfined. For the steady-state simulation (for both cases where the top boundary condition was constant head or no flow), all other layers (i.e., 2 through 55) are treated as confined (i.e., LAYCON=0). For the transient simulations, since pumping can potentially result in aquifer desaturation, we used the CU2 option (i.e., LAYCON=3) for layers 2 through 55. While this option worked well for no flow top boundary condition cases, when using a fixed head top boundary condition, the CU2 option resulted in certain computational cells becoming dry. As **Table 5** indicates, when LAYCON=3 and if the aquifer desaturates, vertical flow from above is not allowed. For this reason, we resorted back to the way layers were treated in steady-state simulations. That is, we assumed all layers, but the first, are all confined. While we were able to model constant head cases using LAYCON=0, it may not be the most physically sound way of simulating pumping events. Especially when, as **Figure 18** illustrates, there is more drawdown under unconfined than the confined conditions. This is either an artifact of the choice of top boundary condition or CU2 allows the aquifer to relax more naturally. Nevertheless, the results imply that a more systematic study of consequences of layer type on the drawdown is warranted.

Another way to represent the groundwater response to pumping is to use several performance measures, as defined by JNC. Such performance measures could be the maximum corrected drawdown (DD_{max}), maximum time at which drawdown occurs ($T_{DD,max}$), and finally the time at which the first derivative of drawdown, with respect to time, yields its maximum value ($\Delta T_{DD,max}$). **Table 6** tabulates such performance measures at various observation and pumping well locations. Clearly, the DD_{max} values occur at the pumping well locations, with the

drawdown at other locations always being negligibly small. However, for the case of pumping above fault, the shallower MIU-1 (i.e., *Z*=-245, -490, and –762 m) and *Z*=-656 m of MIU-2 locations display DD_{max} values that are on the order of a few centimeters. Moreover, we see more significant drawdown for MUI-2 and MUI-3 (e.g., *Z*=-490, -762, and -1025 m), for the case of pumping below the fault. Also, note that at *Z*=-762 m of MIU-2 well, DD_{max} is as high as 3.4 m, since this is actually the pumping well location below the fault. As the table indicates, $T_{DD,max}$ and $\Delta T_{DD,max}$ are generally near the end of the pumping period. This is specially the case when DD_{max} values are significant (e.g., more than a few centimeters).

Figure 19 compares corrected drawdown for the pumping zone below the fault (e.g., similar to those shown in **Figure 17**) with the $|\partial DD/\partial t|$ as a function of time. Here, $|\partial DD/\partial t|$ refers to absolute values of the drawdown derivative with respect to time, *DD* is the drawdown, and *t* is time. **Figure 19** is focused near the end of pumping period, where there is sudden a change in the drawdown and thus $|\partial DD/\partial t|$. While the drawdown appears to be constant as the end of pumping cycle is approached, the oscillation in $|\partial DD/\partial t|$ enhance the small variations in drawdown. At the end of pumping period (i.e., *t*=14 days) $|\partial DD/\partial t|$ yield its maximum value (note that, at *t*=14 days $\partial DD/\partial t$ is actually a negative number and thus, $\partial DD/\partial t$ has a negative minimum at that time). We note that, this time is consistent with $T_{DD,max}$=14 days listed in **Table 6**. However, $\Delta T_{DD,max}$=0.063 days, in the table, refers to the early stages of the pumping where the drawdown gradually increases, before it yields DD_{max}. Finally, during the recovery period (*t*>14 days) both drawdown and $\partial DD/\partial t$ approach zero

Table 6. Performance measures indicating maximum drawdown (DD_{max}), maximum drawdown time ($T_{DD,max}$), and the time at which the first derivative of drawdown with respect to time becomes maximum ($\Delta T_{DD,max}$), for various well locations.

JNC Locations			Model Locations			Pumping Above Fault			Pumping Below Fault		
X	*Y*	*Z*	*X*	*Y*	*Z*	DD_{max}	$T_{DD,max}$	$\Delta T_{DD,max}$	DD_{max}	$T_{DD,max}$	$\Delta T_{DD,max}$
(m)	(m)	(m)	(m)	(m)	(m)	(m)	(days)	(days)	(m)	(days)	(days)
MIU-1											
5488.83	-68629.358	100	5492.34	-68634.26	105	4.708E-05	1.399E+01	4.857E-01	-4.0926E-07	6.2948E-02	1.3967E+01
		-250			-245	1.169E-02	1.398E+01	2.921E-01	-4.2577E-06	2.0836E-01	2.7690E+01
		-500			-490	6.028E-02	1.396E+01	6.295E-02	5.9171E-06	6.2948E-02	1.3967E+01
		-750			-762	4.591E-02	1.400E+01	6.295E-02	-2.4216E-06	2.0836E-01	1.3993E+01
		-1000			-1025	9.824E-04	4.097E+01	8.870E+00	2.8979E-03	3.4186E+01	6.1482E+00
MIU-2											
5433.3	-68552.4	-757.25	5433.29	-68552.40	-762	2.407E-05	2.159E+01	1.399E+01	3.4262E+00	1.4000E+01	6.2948E-02
		-748.1									
		-737.25			-733	5.346E-03	2.087E+01	4.292E+00	3.3630E-01	1.4000E+01	2.0000E+00
		-645.1			-656	1.692E-01	1.400E+01	2.000E+00	6.7937E-03	2.0874E+01	5.2689E+00
		-32.8			-45	1.341E-04	1.382E+01	4.857E-01	8.2532E-07	2.9214E-01	4.0970E+01
MIU-3											
5430.23	-68455.29	100	5433.29	-68443.17	105	5.157E-05	1.379E+01	4.857E-01	4.4477E-06	6.2948E-02	1.4000E+01
		-250			-245	2.089E-03	1.414E+01	3.206E+00	1.6275E-04	5.0000E+01	2.4208E+01
		-500			-490	2.034E-06	2.238E+01	1.396E+01	2.8286E-02	1.3957E+01	2.9214E-01
		-750			-762	-2.146E-06	2.421E+01	1.396E+01	9.8270E-02	1.3985E+01	6.2948E-02
		-1000			-1025	-8.097E-06	2.769E+01	1.399E+01	3.1774E-02	1.3957E+01	2.0000E+00
DH-2											

6708.80	-69474.14	100	6721.64	-69487.10	105	1.890E-06	1.393E+01	1.355E+01	8.4782E-07	1.3219E-01	1.3818E+01
		-250			-245	7.034E-05	1.442E+01	2.000E+00	1.0705E-07	6.2948E-02	1.3945E+01
		-500			-490	3.330E-04	1.487E+01	2.000E+00	-7.2928E-06	6.2948E-02	1.3945E+01
		-750			-762	6.591E-04	1.498E+01	2.000E+00	5.4621E-06	1.3219E-01	1.4000E+01
		-1000			-1025	8.012E-04	1.525E+01	3.206E+00	2.5993E-06	1.3219E-01	1.3967E+01
DH-4											
4343.19	-69602.44	100	4337.05	-69605.38	105	1.153E-06	1.396E+01	1.395E+01	-4.7817E-07	1.3957E+01	1.3993E+01
		-250			-245	1.518E-04	1.398E+01	2.000E+00	2.1289E-06	1.3957E+01	1.3902E+01
		-500			-490	4.115E-04	1.400E+01	2.000E+00	7.8052E-06	1.4000E+01	1.3945E+01
		-750			-762	5.794E-04	1.399E+01	2.000E+00	5.7548E-06	7.1986E-01	1.4000E+01
		-1000			-1025	6.141E-04	1.399E+01	2.000E+00	9.9803E-07	1.3993E+01	1.3985E+01
DH-9											
5782.66	-67206.51	100	5771.44	-67207.12	105	-1.073E-07	1.392E+01	1.390E+01	6.1636E-06	1.3918E+01	1.3902E+01
		-250			-245	1.659E-06	1.397E+01	1.396E+01	4.2226E-04	1.3985E+01	2.0000E+00
		-500			-490	9.176E-06	1.395E+01	1.393E+01	1.1526E-03	1.4865E+01	2.0000E+00
		-750			-762	-1.068E-06	1.498E+01	1.396E+01	1.7046E-03	1.4865E+01	2.0000E+00
		-1000			-1025	5.323E-06	1.393E+01	1.397E+01	1.9314E-03	1.4983E+01	2.0000E+00
TH-8											
4742.51	-68140.01	200	4735.45	-68150.42	190	9.812E-06	1.384E+01	1.400E+01	2.2652E-05	1.3993E+01	2.0000E+00
		100			105	-1.349E-05	1.388E+01	1.400E+01	1.1510E-05	1.3760E+01	2.0000E+00
Well Screens											
Above fault			5433.00	-68552.40	-554.5	9.121E-01	1.399E+01	6.295E-02	7.1516E-06	2.0836E-01	1.3918E+01
					-579.5	9.836E-01	1.399E+01	6.295E-02	7.6889E-06	2.0836E-01	1.3957E+01
					-604.5	1.078E+00	1.398E+01	6.295E-02	-4.7751E-06	2.0836E-01	1.3957E+01
					-629.5	1.072E+00	1.398E+01	6.295E-02	-5.5656E-06	2.0836E-01	1.3864E+01
Below fault					-762	2.407E-05	2.159E+01	1.399E+01	3.4262E+00	1.4000E+01	6.2948E-02

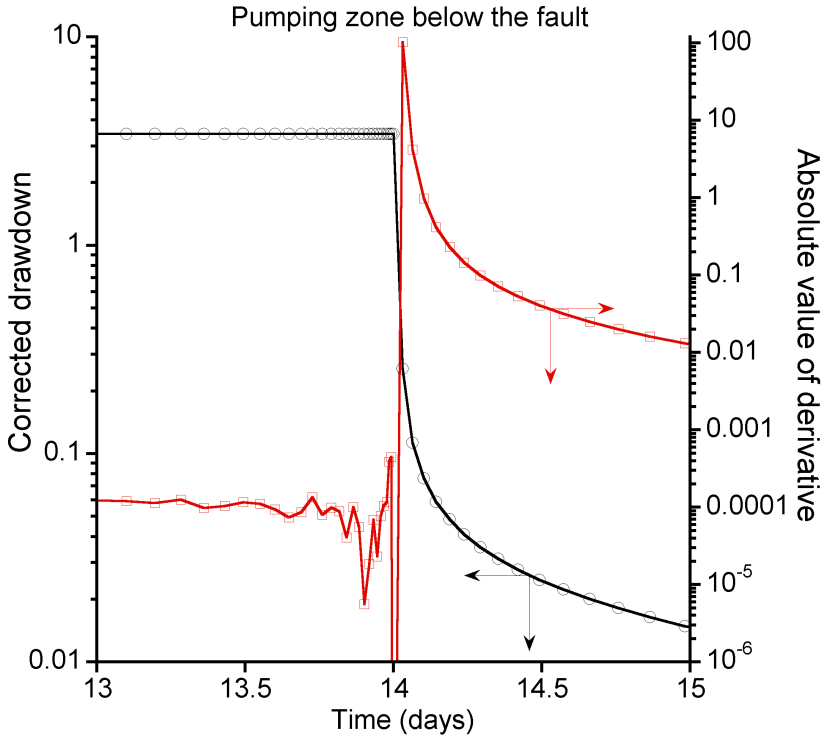

Figure 19. Temporal variation of the corrected drawdown and its comparison to its derivative with respect to time for the pumping zone below the fault. The figure is focused near the end of the pumping period (i.e., t=14) and the onset of the recovery period to illustrate where the derivative experiences its largest change.

Illustrative Particle Tracking for LTPT

In order to determine the control volume affected by 14 days of pumping, we also conducted a series of forward and backward particle tracks. **Figure 20** shows backward tracking, for the simulation with no-flow top boundary condition, and pumping at the well zone above the fault. The figure indicates that the extent of the pumping influence is only within 10-20 m, which is consistent with the extent of the calculated drawdown. In general, however, particle velocity, travel time, and thus the distance traveled by particles are directly affected by the media porosity. As an illustration, we uniformly changed the porosity by one and then two orders of magnitude and performed both forward and backward particle tracking. **Figure 21** depicts the backward particle tracks, originating from the pump below the fault for three different porosity values. It is

clear that reduction in porosity increases the particles' path lengths (note that we have varied the scale in the figures for each case). For instance, considering that the upper pumping zone is 100 m long, the particles for the baseline porosity value only move 10-20 m. However, a 10% porosity reduction increases the maximum path length to ~150 m, and finally a 100% porosity reduction raises the path line lengths by roughly 4 folds (i.e., ~400 m). These simulations demonstrate that the water being supplied to the lower pumping interval is being pulled vertically down along the north side of the fault.

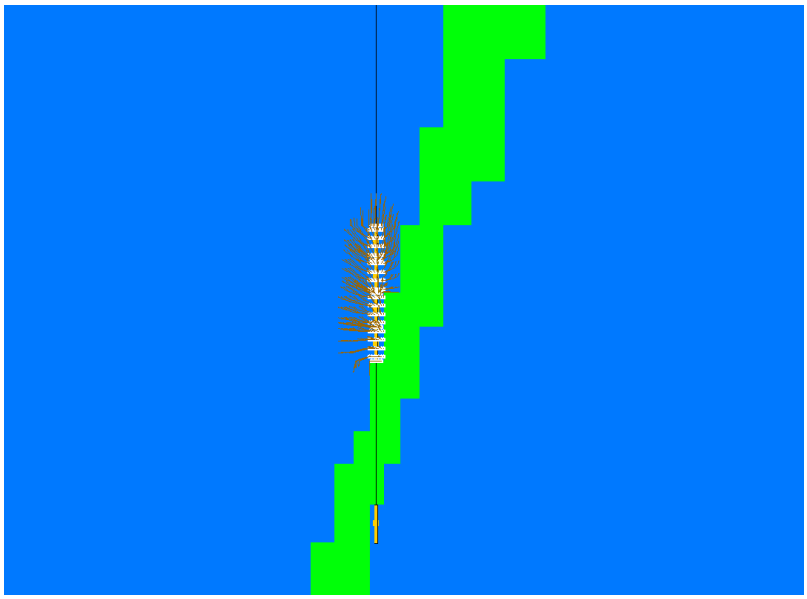

Figure 20. Typical backward particle tracking for a number of particles released from the pumping zone above the fault, for the no flow top boundary condition. Note that the maximum lengths of the path lines are consistent with the maximum zone of influence for the draw down (i.e., 10-20 m). Note that the figure is zoomed to near the pumping location to better illustrate the path lines

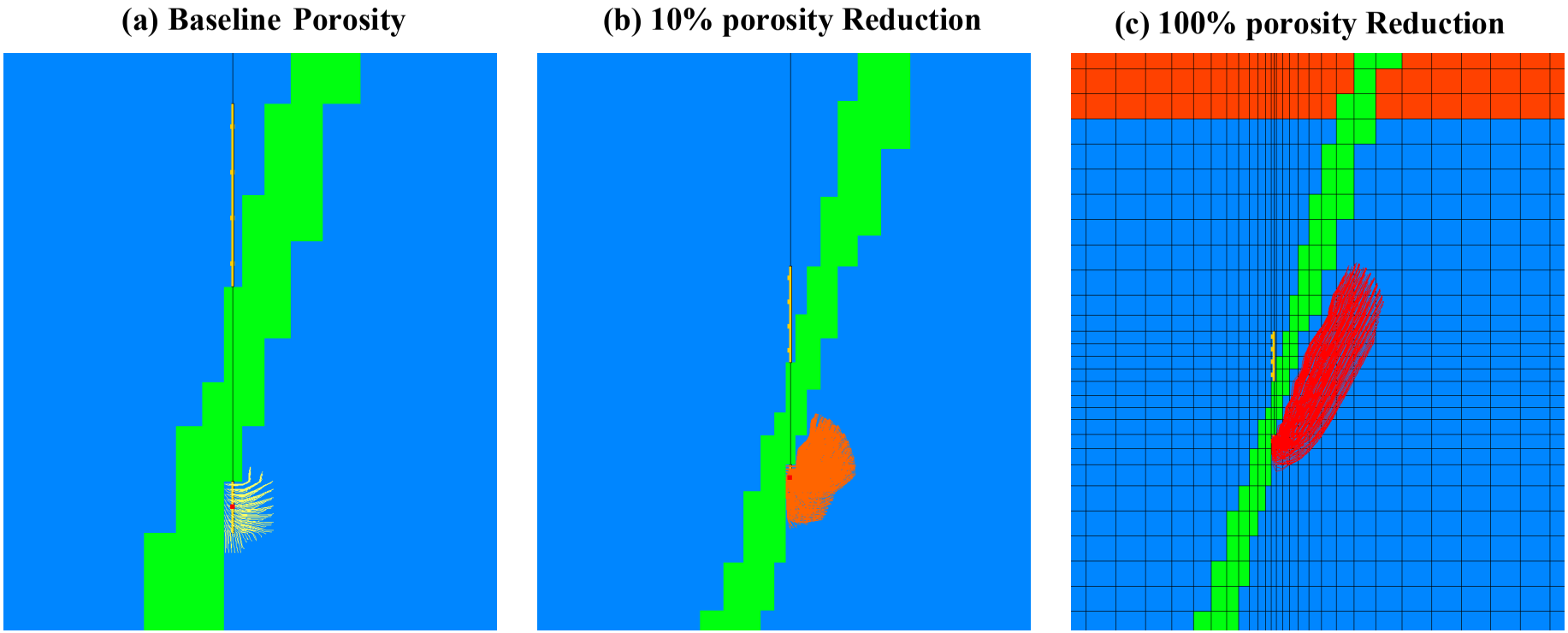

Figure 21. Close up views of the backward particle tracking started from the pumping zone below the fault, illustrating the effect of porosity reduction: a) baseline porosity value results path lengths on the order of 10-20 m, b) an order of magnitude reduction increases the path lines to roughly 150 m, and c) two orders of magnitude reduction in porosity increases the maximum path length to ~400 m. Note that for each case, as the baseline porosity is decreased, the figure is further zoomed out, which can be clearly seen through the thinning of the fault widths.

As a final comparison, **Figure 22** presents forward particle tracks for the baseline and two other porosity values. While the path lines for the baseline porosity values are barely visible (**Figure 22a**), a 10% reduction extends the particle path lines to a few meters (**Figure 22b**). Yet, a 100% reduction in the porosity (**Figure 22c and d**) increases the path line lengths to 100s of meters. We should, however, be cautious here. Since we generated the initial head fields using the baseline porosity values, the shape of the particle trajectory, in **Figure 22**, are generally due to the original baseline model. That is, by reducing the porosity we have artificially increased the trajectory distance and not the intrinsic nature of the path lines.

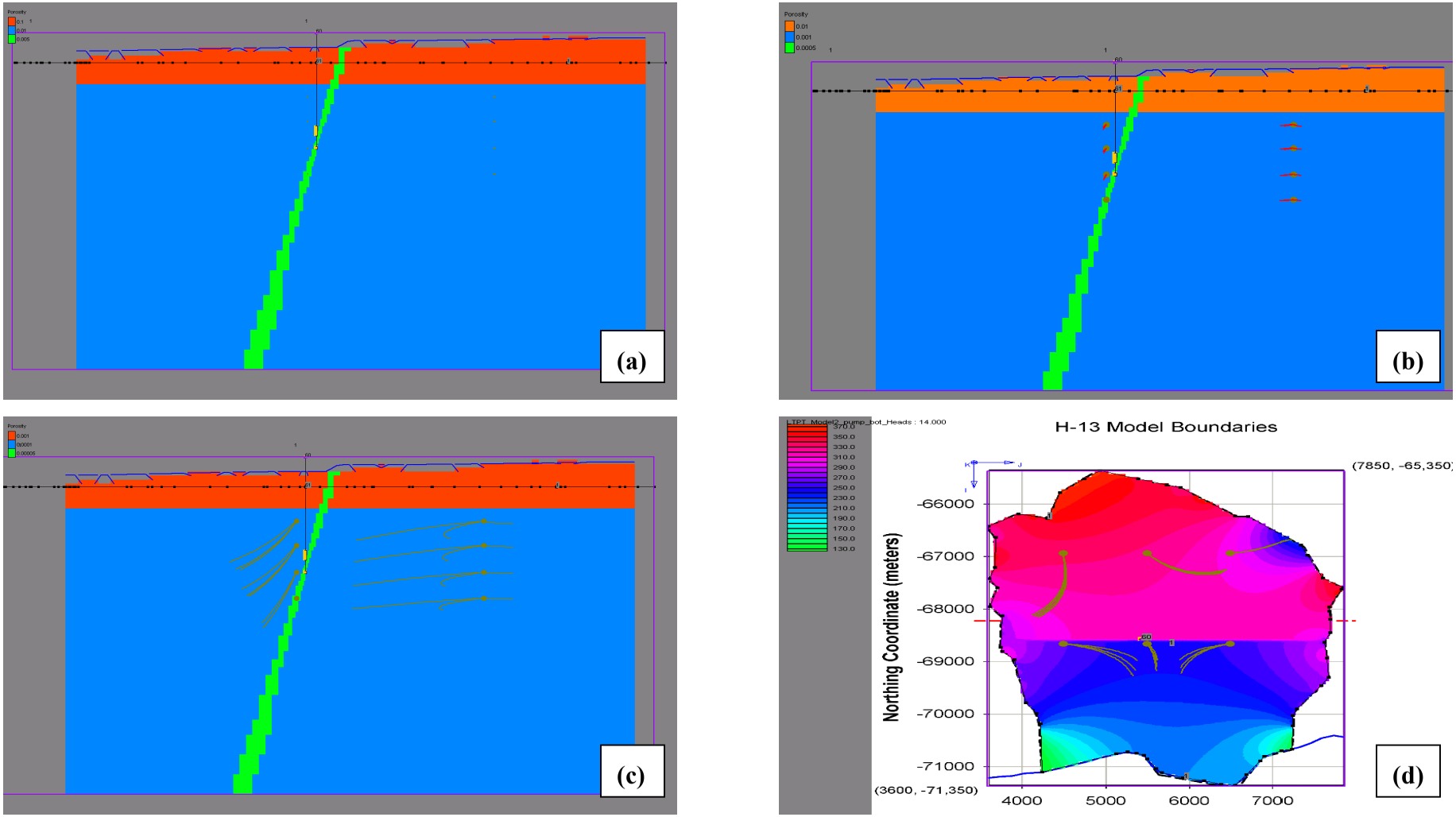

Figure 22. Forward particle tracks illustrating the effect of artificial porosity reduction on the path lengths: a) path lines using the baseline porosity values show near negligible movement away from where the particles are released from, b) a uniform reduction of 10% in porosity increases the path lengths to several meters, c) decreasing the baseline porosity further (e.g., 100% reduction) increases the path lengths to 100s of meters, and d) shows the plan view of the path lines for the case shown in c.

Conclusions

A conceptual model of MIU site, located near the town of Mizunami City in the Gifu Prefecture northeast of Nagoya City, Japan, was developed to predict the groundwater system response to pumping. The study area consisted of a fairly large three-dimensional domain, having the size 4.25 x 6 x 3 km^3. The model also consisted of three different geological units, upper and lower fractured zones and a single fault unit. The resulting computational model comprised of 702,204 finite difference cells with variable grid spacing, where the underlying mesh was generated using the GMS software (GMS, v3.1, 2000). GMS was also used to build the entire model including the pumping well locations and assignment the various aquifer properties (e.g., hydraulic conductivity, storage coefficient, specific storage, and porosity (for particle tracking)).

The resulting flow field, which was obtained using MODFLOW (McDonald and Harbaugh, 1988) package, included both a series of steady state and transient simulations. In general, while the steady state simulations required less than 20 minutes of CPU time on a 450 MHz PC, the transient simulations depending upon the extent of the pumping and recovery period, required more CPU time. Nevertheless, the total simulation time never exceeded 2 hrs on a 450 MHz PC. For both steady state and transient simulations, the influence of the surface boundary condition, subject to a fixed head and no flow conditions, were considered and recharge was not considered in this work. Steady state results were used for particle tracking and also serving as the initial conditions (i.e., starting heads) for the transient simulations.

Results of the steady state simulations clearly indicate the significance of the choice of surface (i.e., upper) boundary conditions. For instance, when the upper boundary is a fixed head condition, the pressure gradient near the surface that varies with the elevation, results in a net flux into the system. This is quite similar to imposing an implicit recharge and is clearly seen in the flow patterns at the base of the upper fractured zone. However, when the upper boundary is changed to a no condition, the head fields are continuous across the upper and lower fractured zones, indicating negligible gradient and thus little to no flux crossing the two geological units.

Steady state particle tracking results clearly illustrate that all particles released, from the points defined by JNC, exit the top of the model in areas where groundwater discharge is along the Shoba and Toki rivers. These particles all reach the top of the model well north of the southern no-flow boundary. Only two of the particles (13 and 19) exit the model far enough to the south to experience any effect of the southern no-flow boundary. In addition, the steady state particle travel times range from 3.6×10^7 sec (i.e., ~1.1 years) for particle 15 to 4.4×10^{10} sec (i.e., ~1394 years) for particle number 22. Meanwhile, particle 13, which was located at the top north left, had the longest travel distance of 3232 m, and particle 15 only traversed a distance of 501 m - the shortest distance traveled.

For the transient simulations (i.e., pumping), two pumping zone one above and another one below the fault are considered. For both cases (i.e., pumping above and below) the fault, the pumping period extends for 14 days followed by an additional 36 days of recovery. Separate cases for the pumping above and below the fault are also considered. We find, in general, for the pumping rates used, the maximum drawdown is quite small (ranging from a few centimeters to a few meters) and thus, pumping does not severely impact the groundwater response. We also found, the range of drawdown values produced by pumping below the fault are generally much less sensitive to the choice of the boundary condition than are the drawdowns resulted from the pumping zone above the fault. However, we found the choice of boundary condition for the top of the model to also influence predicted drawdowns. The effect of the boundary conditions under the transient situation deserves a closer look and probably needs more exploration.

References

Anderson, M. P. and W. M. Woessner, Applied Groundwater Modeling: Simulation of Flow and Transport, Academic Press, New York, New York, USA, 1992.

Domenico, P. A. and F. W. Schwartz, Physical and Chemical Hydrogeology, John Wiley and Sons, Inc., USA, 1990.

Freeze, R. A. and J. A. Cherry, Groundwater, Prentice-Hall, Inc., New Jersey, USA, 1979.

GMS, v3.1, The Department of Defense Groundwater Modeling System, Brigham Young University-Environmental Modeling Research Laboratory, 2000.

Harbaugh, A. W. and M. G. McDonald, User's documentation for MODFLOW-96, an update to the U.S. Geological Survey modular finite-difference ground-water model, U.S. Geological Survey, Open-File Report 96-485, Reston, Virginia, 1996.

Martinez, M. J., P. L. Hopkins and P. C. Reeves, PorSalsa User's Manual, *SAND2001-1555*, Sandia National Laboratories Tech. Rept., Albuquerque, New Mexico, 2001.

McDonald, M. G. and A. W. Harbaugh, A Modular Three-dimensional finite-difference ground-water flow model, Book 6, Modeling Techniques, Scientific Software Group, Washington, D.C., 1988.

McKenna, S. A., M. Eliassi, K. Inaba, and H. Saegusa, Evaluation of uncertainties due to hydrological modeling and groundwater flow analysis (part 5)- Groundwater flow modeling focused on complexity in the interpreted fault network using POR-SALSA, in proceedings of Groundwater Flow in Discrete Fractures Symposium, *Japanese Geotechnical Society*, Tokyo, September 10-11, 2001.

Pollock, D. W., User's Guide for MODPATH/MODPATH-PLOT, Version 3: A particle tracking post-processing package for MODFLOW, the U.S. Geological Survey finite-difference ground-water flow model, U.S. Geological Survey, Open-File Report 94-464, Reston, Virginia, 1994.

Prichett, J. W. and S. K. Garg, Determination of effective well block radii for numerical reservoir simulations, *Water Resour. Res.*, *16*(4), pp. 665-674, 1980.

Distribution:

Number of copies	Mail Stop	Name	Organization
3	735	Susan Altman	6115
5	735	Mehdi Eliassi	6115
1	735	Scott James	6115
3	735	Sean McKenna	6115
1	735	David Miller	6115
1	719	Susan Howarth	6131
10	731	NWM Library	731
1	8945	Central Technical Files	9018
2	899	Technical Library	9616
1	612	Review and Approval Desk for DOE/OSTI	9612